



ICT-777137

5G-RANGE

5G-RANGE: Remote Area Access Network for the 5th Generation

Research and Innovation Action
H2020-EUB-2017 – EU-BRAZIL Joint Call

Deliverable 3.1 Physical layer of the 5G-RANGE – Part I

Due date of deliverable: 31st October 2018
Actual submission date: 21st December 2018

Start date of project: 1st November 2017
Duration: 30 months
Lead contractor for this deliverable: UFC
Version 1 date 21st December 2018
Confidentiality status: Public

Abstract

The current technical report describes the 5G-RANGE channel models and their correspondence with the defined use cases. A discussion about possible waveforms and their advantages/disadvantages is also included. Finally, the channel coding/decoding schemes, namely the 5G-ACRA (Advanced Coding for Remote Areas), are also presented, targeting the different aspects of the PHY layer.

Target audience

The primary target audience for this document is the radio access network research and development community, particularly those with an interest in mobile communication physical and MAC layers. This material can be fully understood by readers with a background in mobile wireless cellular systems, especially those familiar with 3GPP standards for 4G and 5G networks.

Disclaimer

This document contains material, which is the copyright of certain 5G-RANGE consortium parties and may not be reproduced or copied without permission. All 5G-RANGE consortium parties have agreed to the full publication of this document. The commercial use of any information contained in this document may require a license from the proprietor of that information.

Neither the 5G-RANGE consortium as a whole, nor a certain party of the 5G-RANGE consortium warrant that the information contained in this document is capable of use, or that use of the information is free from risk and accept no liability for loss or damage suffered by any person using this information.

This document does not represent the opinion of the European Community, and the European Community is not responsible for any use that might be made of its content.

Impressum

Full project title:	5G-RANGE: Remote Area Access Network for the 5th Generation
Document title:	D3.1 Physical layer of the 5G-RANGE – Part I
Editor:	Bruno Sokal, UFC (BR)
Work Package No. and Title:	WP3, Physical layer of the 5G-RANGE
Work Package leaders:	Peter Neuhaus, TUD (EU), Luciano Mendes, Inatel (BR)
Project Co-ordinators:	Marcelo Bagnulo, UC3M (EU), Priscila Solis, UnB (BR)
Technical Manager:	Luciano Mendes, Inatel (BR)

Copyright notice

© 2018 Participants in project 5G-RANGE

Executive Summary

The channel models and the system requirements are the primary information necessary for designing the cognitive MAC and physical layers for 5G-RANGE network. One of the main objectives of this document is to describe the channel models associated with the core use cases requirements listed in D2.1. Due to the large radius of a 5G-RANGE cell, the channel model is divided into two categories: general case and D2D, where for both, measurements in the literature were considered for a formal proposition in the 5G-RANGE context. In order to increase the scope of this report, channel models for IEEE 802.22 and DTV are also included and briefly analyzed. This report also presents possible waveforms for the physical layer, highlighting the advantages and disadvantages of each approach. Finally, the report brings a discussion about the coding schemes selected for forward error control. The performance of the channel coding schemes is analyzed and solutions for the 5G-RANGE are proposed.

Perspectives for the next deliverable D3.2 “Physical Layer of the 5G-RANGE – Part: 2” are discussed in order to improve the performance of the proposed models described in this document.

List of Authors

Bruno Sokal (UFC)

Alexandre Matos (UFC)

Carlos Silva (UFC)

Tarcisio Maciel (UFC)

Yuri Silva (UFC)

André Almeida (UFC)

Danilo Gaspar (INATEL)

Luciano Mendes (INATEL)

Peter Neuhaus (TUD)

Wheberth Dias (INATEL)

Table of Contents

Executive Summary	3
List of Authors	4
Table of Contents	5
List of figures	7
Definitions and abbreviations.....	10
1 Introduction	12
2 Channel Characterization	13
2.1 Channel characterization for extreme rural areas	14
2.1.1 General Case.....	14
2.1.2 D2D	17
2.2 Channel generation.....	19
2.3 Simulations Results	22
2.4 Delay profile characteristics of other channel models.....	25
2.5 Discussions and Future Perspectives.....	26
3 5G-RANGE Waveforms	28
3.1 OFDM	28
3.1.1 OFDM waveform description.....	28
3.1.2 OFDM advantages and disadvantages.....	28
3.2 F-OFDM.....	29
3.2.1 F-OFDM waveform description	30
3.2.2 F-OFDM advantages and disadvantages	30
3.3 GFDM	31
3.3.1 GFDM Waveform Description.....	31
3.3.2 GFDM advantages and disadvantages.....	32
3.4 B-OFDM	33
3.4.1 B-OFDM Waveform Description.....	33
3.4.2 B-OFDM advantages and disadvantages.....	34
3.5 Discussion and Future Perspectives	34
4 Channel coding for 5G-ACRA	36
4.1 Turbo codes	37
4.2 LDPC codes.....	38
4.3 Polar codes	39
4.4 Forward error correction performance	40
4.4.1 Simulation Framework	41

4.4.2	Performance analysis.....	41
4.5	Complexity comparison	46
4.6	Discussion and Future Perspectives	47
5	EU projects on 5G PHY.....	49
6	Conclusions	50
7	References	51
Annex A		54
Annex B		55
Annex C		57

List of figures

Figure 1. 5G-RANGE cell.....	13
Figure 2. Measured data and the proposed path loss model for the 5G-RANGE project.	15
Figure 3. Estimated Shadow Fading standard deviation: (a) without removing the outliers. (b) after removing the outliers.....	16
Figure 4. Comparison between Rural Macro 3GPP TR 38.901 and the proposed path loss model.....	16
Figure 5. Path loss models proposed by [8] and equivalent/combined path loss model (black line). ...	18
Figure 6. CDF of measured path loss in Figure 2.....	24
Figure 7. Channel Throughput for a Tx power of 49dBm, NLOS case.	24
Figure 8. Channel Throughput for a Tx power of 53dBm, NLOS case.	25
Figure 9. Channel Throughput for a Tx power of 49dBm, LOS case.	25
Figure 10. Channel Throughput for a Tx power of 53dBm, LOS case.	25
Figure 11. OFDM modulator and demodulator block diagram.....	28
Figure 12. OFDM spectrum and its OOB emissions.....	29
Figure 13. Cyclic prefix overhead in OFDM.	29
Figure 14. F-OFDM downlink block diagram.	30
Figure 15. F-OFDM spectrum with reduced OOB emissions.....	31
Figure 16. GFDM modulator and demodulator block diagram.....	32
Figure 17. GFDM symbol structure as a time-frequency grid.	32
Figure 18. PSD comparison of OFDM and GFDM.	33
Figure 19. B-OFDM block structure.	33
Figure 20. B-OFDM modulator and demodulator block diagram.....	34
Figure 21. Structure of rate 1/3 turbo encoder as specified in [24].	37
Figure 22. Simplified overview of the parity check matrix structure of the 5G NR base graphs.	39
Figure 23. Channel polarization for $N = 2$	40
Figure 24. BLER performance comparison of Polar, LDPC and Turbo code for BPSK over AWGN.	42
Figure 25. BLER performance comparison of 5G NR Polar and LDPC code for BPSK over AWGN.	42
Figure 26. BLER comparison of 5G NR Polar and LDPC code for a code rate of $R = 2/3$ and different block sizes.....	43
Figure 27. Evaluation of the BLER performance of the SCL Polar decoder and the SPA LDPC decoder for different list sizes and number of iterations, respectively. Results are obtained for 100,000 blocks of length 1024/1056 with code rate 2/3 for BPSK modulation over an AWGN channel.	44
Figure 28. Comparison of QAM SER for Polar and LDPC code with different block sizes for GFDM modulation over an AWGN channel. As expected, the SER is independent of the channel code as well as the block size. Note that all curves are perfectly overlapping.	45
Figure 29. Comparison of BER for Polar and LDPC code with different block sizes for GFDM modulation over an AWGN channel.	46

Figure 30. Comparison of BLER for Polar and LDPC code with different block sizes for GFDM modulation over an AWGN channel.	46
---	----

List of tables

Table 1. Coefficients from the scenarios in [7].	17
Table 2. Offset to each ray within a cluster.	22
Table 3. Simulation parameters.	22
Table 4. Maximum excess delay of other channel models.	26
Table 5. 5G-ACRA specifications.	36
Table 6. Overview on the channel coding schemes for 5G NR channels [25]. The uplink and downlink control information channels are denoted by UCI and DCI, respectively. UL-SCH and DL-SCH denote the uplink and downlink shared channels and PCH and BCH denote the paging channel and broadcast channel, respectively.	37
Table 7. Supported code rates and block sizes for 3GPP 5G NR base graph (BG) 1 and 2.	38
Table 8. Simulation parameters for comparison of Polar, LDPC and Turbo codes.	41
Table 9. Overview on the compared block sizes for Polar and LDPC codes.	43
Table 10. Overview on the GFDM simulation settings.	45
Table 11. CDL-A model with scaled delays and angles for the general case.	55
Table 12. CDL-D with scaled delays and angles for the general case.	56
Table 13. CDL-A with scaled delays and angles for D2D.	57
Table 14. CDL-D with scaled delays and angles for D2D.	58

Definitions and abbreviations

5G-ACRA (5G Advanced Coding for Remote Areas).....	36
5G-FlexNOW (5G Flexible Non-Orthogonal Waveforms).....	28
5G-LA (5G Link Adaption)	36
5G-MIMORA (Multiple-Input Multiple-Output techniques for Remote Areas applications).....	12
5GNOW (5th Generation Non-Orthogonal Waveforms for Asynchronous Signalling)	34
ASA (azimuth spread of arrival)	15
ASD (azimuth spread of departure).....	15
BER (bit error rate).....	44
BFDM (Biorthogonal Frequency Division Multiplexing).....	34
BLER (block error rate)	41
B-OFDM (block OFDM)	33
CA-Polar (CRC-aided Polar).....	40
CDL (clustered delay line)	15
CIR (channel impulse response).....	33
CPE (Customer Premises Equipment)	13
D2D (Device to Device).....	14
DS (delay spread)	15
FBMC (Filter Bank Multi-Carrier).....	34
FDE (frequency domain equalizer)	34
FEC (forward error correction)	36
FFT (fast Fourier transform)	28
F-OFDM (filtered OFDM)	29
FSPL (free space path loss)	14
GFDM (generalized frequency division multiplexing)	31
gNB (next generation eNodeB).....	31
ICI (intercarrier interference)	30
IR-HARQ (incremental redundancy hybrid automatic repeat request).....	39
ISI (intersymbol interference)	30
KPI (key performance indicator).....	26
LDPC (low-density parity-check)	36
LLR (log-likelihood ratio).....	40
LOS (Line of Sight).....	15
LS (Least Squares)	17
LTE (Long Term Evolution)	36
MCS (modulation and coding scheme)	48
METIS (Mobile and wireless communications Enablers for the Twenty-twenty Information Society).....	49
MF (matched filter)	31
MIMO (Multiple-Input Multiple-Output)	12
MMSE (Minimum Mean Square Error)	15
MSA (min-sum-algorithm).....	47

NLOS (No Line of Sight).....	15
NR (new radio).....	36
OFDM (orthogonal frequency division multiplexing)	28
PHY (physical layer).....	36
PoE (probability of error)	39
PRB (physical resource block).....	23
PSD (power spectrum density).....	31
QAM (quadrature amplitude modulation).....	28
QC-LDPC (quasi-cyclic LDPC).....	38
RAN (radio network access)	49
RC (raised cosine)	32
RMS (root mean square)	14
SC (successive cancelation)	40
SC-FDE (single-carrier frequency domain equalization).....	32
SCL (successive cancelation list).....	40
SER (symbol error rate)	44
SISO (Single-Input Single-Output).....	23
SNR (signal to noise ratio)	31
SPA (sum-product-algorithm)	41
TVWS (TV White Space)	12
UE (User Equipment).....	13
UFMC (Universal Filtered Multi-Carrier),.....	34
ZF (zero forcing)	31
ZSA (zenith spread of arrival).....	15
ZSD (zenith spread of departure)	15

1 Introduction

The next generation of mobile networks, 5G, shall not only bring higher data rates and more reliable communications, but also device connection will be a feature of this network generation. Nevertheless, these features are usually addressed to urban areas where a high user density is expected. In order to attract the investment to rural areas from the companies, the 5G-RANGE project adopts the use of sharing spectrum in TVWS (TV White Space) where the secondary users (e.g., mobile devices) share the VHF and UHF channels with the primary users (e.g., TV broadcaster). The use of shared spectrum is a challenging task in order to avoid secondary to primary users' interference. Some techniques that will be employed in this project to overcome this issue can be cited as spectrum sensing and an appropriate choice of waveform which can reduce significantly the OOB (out of band) emissions. But, for this, a reliable and coherent channel model for remote/rural areas and a good match of channel coding (5G-ACRA) must be provided.

The technical sections of the document are organized as follows:

- Section 2: This section discusses some channel models for 5G networks in the literature and provides two models for different link distances, whereas both models rely on measurements performed by the literature. Also, a step-wise guideline how to generate the proposed channel is provided. Finally, channel capacity simulations are discussed;
- Section 3: A detailed review discussing the advantages and disadvantages of the main waveforms that are being considered in the 5G-RANGE project is given;
- Section 4: This section describes the channel coding for the 5G-ACRA. Also, it is provided a deep analysis using AWGN channels, comparing Turbo, LDPC and Polar codes in terms of performance (Block Error Rate), size of coding block and complexity;
- Section 5: Here, a brief discussion about the past and current EU projects that have contributed for the 5G PHY layer development is presented.

In addition, for the next deliverable D3.2 “Physical Layer of the 5G-RANGE – Part: 2” some extensions of this deliverable shall be presented, e.g., the 5G-ACRA performance analysis with the proposed channel model of Section 2, a proposed waveform for the 5G-FlexNOW (Flexible Non-Orthogonal Waveform modulator/demodulator) and improvements of the channel capacity using MIMO (Multiple-Input Multiple-Output) schemes for diversity, multiplexing and beamforming in 5G-MIMORA (Multiple-Input Multiple-Output techniques for Remote Areas applications).

2 Channel Characterization

This section discusses and presents a channel model for rural/remote areas for the 5G-RANGE project. As will be presented later in this section, the models available in the literature cannot be directly applied in the 5G-RANGE project context, due for frequency, cell radius and/or channel bandwidth. Figure 1 illustrates the different links that will be discussed in this document. According to [1], a CPE (Customer Premises Equipment) is a fixed device in the network that helps the UE (User Equipment) located at the cells edge (or near to cells edge) to transmit to the BS (Base Station), i.e., it can also act as a relay station. Therefore, throughout this document, a CPE is considered to be a relay station.

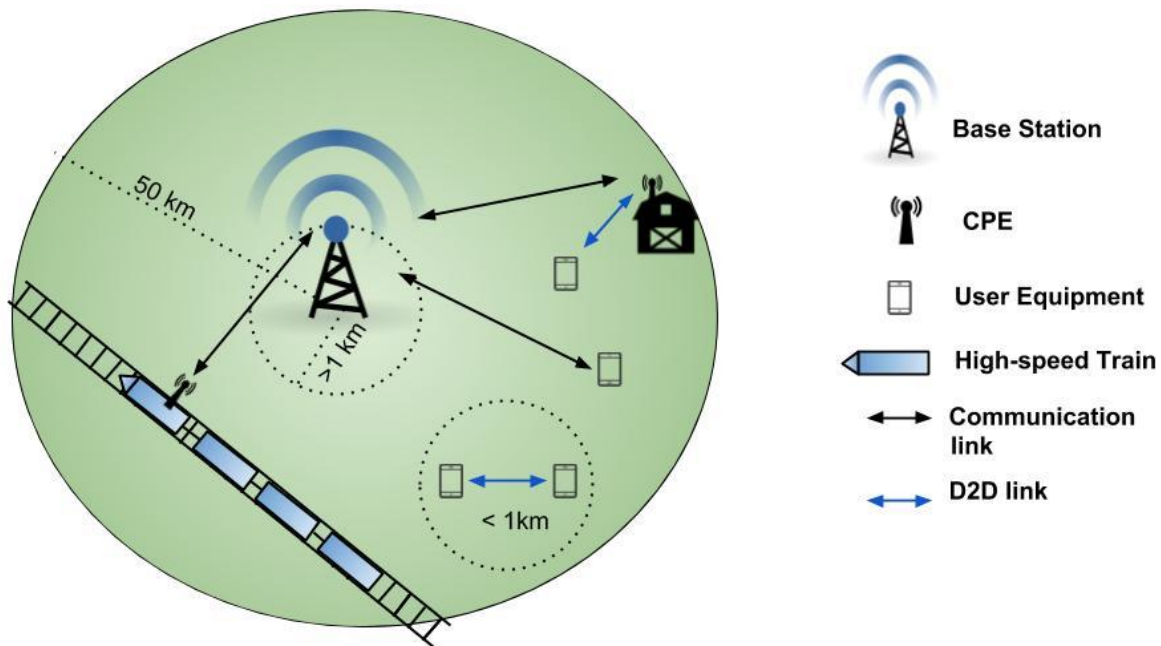


Figure 1. 5G-RANGE cell.

In this document, a channel model is specified for the following scenarios:

- **BS to UE (downlink) and UE to BS (uplink) or UE to CPE to BS (uplink) (case where the UE is located too far from the BS):**
 - Low mobility (UE with speed around 3 km/h);
 - Throughput of 100 Mbps at the cell border (considering no mobility and all resources allocated to a single UE).
- **High-speed user: BS to UE (downlink) and UE to BS (uplink)**
 - The UE is located in a high-speed transport, e.g., train with speed around 120 km/h;
 - High Doppler effect.
- **D2D (Device to Device) communications, i.e., UE to UE (downlink and uplink), UE-CPE:**
 - Low mobility;
 - Distances of few hundred meters.
- **Real-time monitoring of farm machinery, i.e., BS to UE (downlink) and UE to BS (uplink), or UE to CPE to BS (uplink):**
 - Use of smart truck or tractors;
 - Low-Latency;
 - Predictive and preventive maintenance.

It is important to mention that the proposed channel model is for outdoor environments. For the indoor case, a 4G/5G small cell or other technologies, such as Wi-Fi, can be employed. Also, the presented scenarios are related with the core use cases of the 5G-RANGE project, described in deliverable D2.1 “Applications and Requirement report” [1].

2.1 Channel characterization for extreme rural areas

The channel characterization for remote/rural large areas is not a simple task, as there are many channel models for 5G networks, such as the 3GPP TR 38.901 [2], METIS-II project (metis-ii.5g-ppp.eu), and the QuaDRiGa [3]. However, none of these models have been validated for extreme rural distances and cannot be directly applied to the 5G-RANGE scenario. Moreover, for the path loss model, there are many models in the literature that can be applied to a large range of frequencies and distances, such as Longley&Rice model, ITU-P-1546, ITU-R-525 and Hata-Davidson model which is an extension of the well-known Okumura-Hata model to distances up to 300 km. Nevertheless, for these path loss models, a lot of parameters, such as the HAAT (height above average terrain), must be set, while for the 5G-RANGE, a simple path loss model, based on measurements in literature, is proposed.

In [4], a measurement campaign was performed by Ericsson and Telstra for extreme rural scenarios on 3G live cells (band 5: 850 MHz), with distances up to 200 km. In [5] and [6], a path loss and fast fading model are proposed, based on these measurements. These works are the main reference for the proposed channel model for the general case (links from 1 km to 50 km). The links with distances between 20 m and 1 km are characterized as a D2D model.

In [7], a path loss model for D2D (Device to Device) communications in a rural environment is presented based on measurements. In the context of 5G-RANGE project, such model is also used, but with some adjustments described in the next sections.

The proposed channel models consider two different cases:

- **General case:** For BS-UE, UE-BS, BS-CPE and CPE-BS links, with distances between 1 km and 50 km.
- **D2D case:** For UE-UE, UE-CPE links, with distances between 20 m and 1 km.

These two cases will be discussed in detail following.

2.1.1 General Case

As mentioned in the previous section, in [4], a measurement campaign was performed by Ericsson & Telstra for extreme rural areas in order to model the path loss and the RMS (root mean square) with a different terrain profile. The relative height difference between UE and the BS was between 500 m and 600 m. This means that the BS is located at the top of a hill or in an elevated spot, which will be the case in the 5G-RANGE cell. From these measurements, two works were derived to characterize the channel model for extreme rural areas. In [5], the large-scale model was described, while [6] presents the fast fading model.

Starting with the work in [5], the authors proposed a simple path loss model, given by

$$PL(d)[\text{dB}] = \text{FSPL}(d_{\text{km}}, f_{\text{MHz}})[\text{dB}] + K, \quad (1)$$

Where the distances d are in kilometers, frequencies f are in MHz in the FSPL (free space path loss) model and the offset K is a value in dB. It is important to mention that the authors in [5] consider as region of interest $45 \text{ km} < d < 115 \text{ km}$. For this region, in [5], the authors proposed an offset K of 20 dB and a shadowing with a zero-mean and standard deviation σ of 8 dB.

Now, for the fast fading model, the authors of [6] proposed for link and system level simulations the use of CDL (clustered delay line) models from [2], such as the CDL-A, for NLOS (No Line of Sight) case, and CDL-D, for the LOS (Line of Sight) case, with the following scaling parameters:

- DS (delay spread) = 100 ns;
- ASD (azimuth spread of departure) = 1°;
- ASA (azimuth spread of arrival) = 30°;
- ZSD (zenith spread of departure) = 0.1°;
- ZSA (zenith spread of arrival) = 1°.

For the 5G-RANGE project, the proposed path loss is given by (1) for different values of K and shadowing standard deviation σ , in dB. **Error! Reference source not found.** shows the measured data in [4] for different scenarios, considering now the region of interest of the 5G-RANGE project, i.e., $1 \text{ km} < d < 50 \text{ km}$. Using the MMSE (Minimum Mean Square Error) approach, the offset K for the general case is computed as

$$K = \frac{1}{I} \sum_{i=1}^I (y(d_i) - \text{FSPL}(d_i, f)), \quad (2)$$

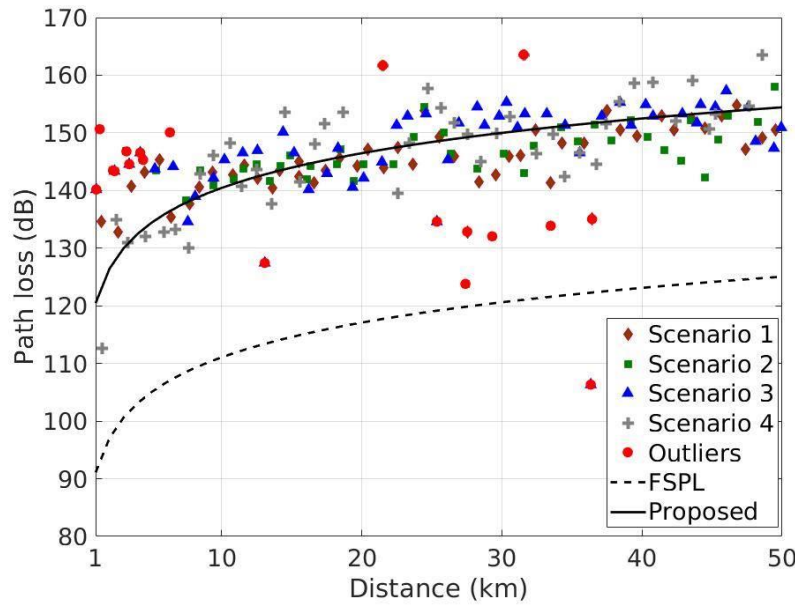


Figure 2. Measured data and the proposed path loss model for the 5G-RANGE project.

where $y(d_i)$ is the measurement data and $I = 191$ is the total number of samples in **Error! Reference source not found.**. It is important to mention that in **Error! Reference source not found.**, each value of the measurement data $y(d_i)$ is in fact a mean of thousands of path loss samples, according to [4]. This leads to a $K = 29.42 \text{ dB}$. Now, for the shadowing, it is computed as

$$SF(d_i) = y(d_i) - \text{PL}(d_i, f), \quad (3)$$

which, in this case, has a standard deviation $\sigma_{SF} = 7.5 \text{ dB}$ (**Error! Reference source not found. (a)**). This value considers all the measurements in **Error! Reference source not found.**. However, as it can be observed, some path loss samples shall be considered as outliers, since they are several dBs “far away” from the proposed path loss. In order to solve this problem, a numerical analysis was performed to choose the interval that best fits the empirical and theoretical shadow fading presented in Figure 3. It was found that the best interval is $[-1.5 \sigma_{SF}, 1.5 \sigma_{SF}]$ and, with that, a total of 19 samples were removed.

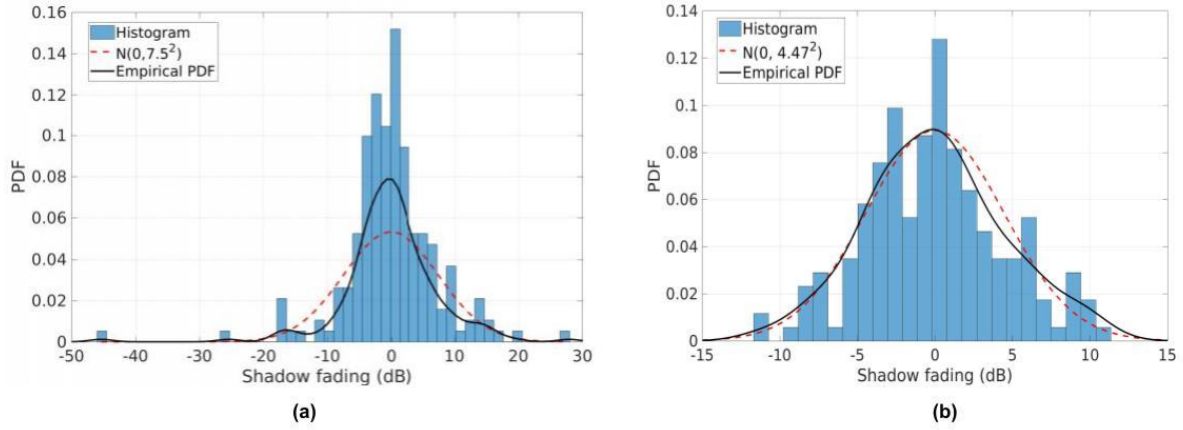


Figure 3. Estimated Shadow Fading standard deviation: (a) without removing the outliers. (b) after removing the outliers.

In **Error! Reference source not found.**, the empirical probability density function (PDF) of the measured data (with and without the outliers) was computed using the kernel smoothing method in [8] and it can be observed that a normal distribution with zero-mean and standard deviation of $\sigma_{SF} = 4.47$ has a better agreement with the data with outliers removed. Now re-computing the offset K , using (2), the data without the outliers yields $K = 29.38$ dB. The outliers' removal does not have a significant impact on the offset K , as it can be seen. However, removing the outliers decreases the standard deviation of the shadowing, in the 5G-RANGE case, leading to a reduction of 3.03 dB.

Thus, for the 5G-RANGE project, the proposed parameters for the general case in (1), are

- $K = 29.38$ dB;
- $\sigma_{SF} = 4.47$ dB.

In **Error! Reference source not found.**, the proposed path loss model is compared with the model in 3GPP TR 38.901, with the following parameters:

- BS height: 150 m;
- UE height: 1.5 m;
- Average building height: 5 m;
- Average street width: 20 m.

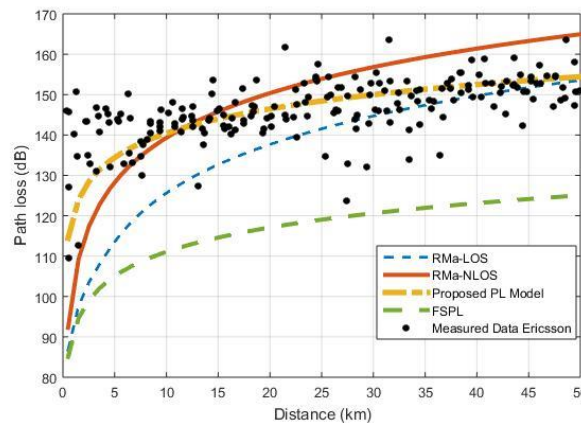


Figure 4. Comparison between Rural Macro 3GPP TR 38.901 and the proposed path loss model.

It can be noticed in **Error! Reference source not found.** that the proposed path loss model approximates better the data measured by Ericsson and Telstra than the one proposed in 3GPP TR. 38.901 [2], for rural macro areas.

In the case of fast fading model for the 5G-RANGE project, it is recommended to follow the proposal of [6], where the authors indicate for link and system level simulation the use of CDL models with the following scaling parameters:

- DS = 100 ns;
- ASD = 1°;
- ASA = 30°;
- ZSD = 0.1°;
- ZSA = 1°.

It is important to mention that the authors in [5] show that the RMS delay spread does not change as function of the distance and, due to the long distances and high effective antenna height, a small angular spread is expected.

2.1.2 D2D

Reference [7] conducted a measurement campaign of path loss considering four different scenarios (named Hewson, Grundy, Follet and Watts) for D2D communication in a rural area. The data were measured in the frequency of 922 MHz and the distances between the transmitter and receiver were from 20 m up to 600 m. The authors proposed a path loss model (frequency independent) given by

$$PL(d_m)[\text{dB}] = PL(d_0) + 10 \cdot \alpha \cdot \log_{10}\left(\frac{d_m}{d_0}\right), \quad d_m \geq d_0, \quad (4)$$

where $PL(d_0)$ is the path loss in dB to the reference distance of $d_0 = 20$ m, α is an attenuation coefficient that measures how fast the path loss increases with the logarithm of the distance. In Table 1, the coefficients of (4), for the scenarios studied in [7], are shown with their respective standard deviation of the shadowing.

Table 1. Coefficients from the scenarios in [7].

	$PL(d_0)$ [dB]	α	σ [dB]
Hewson	46.81	3.55	4.32
Grundy	41.99	4.09	4.36
Follet	52.96	2.97	5.39
Watts	48.40	3.31	4.70

The measured data from [7] was obtained in a rural scenario, but considering different distance ranges and also frequencies. In order to provide a path loss model based on such measurement data to the frequencies from 170 MHz up to 700 MHz (frequency range employed for 5G-RANGE) and distances from 20 m up to 600 m, the proposed path loss model in [7] was rewritten as follows:

- 1) The coefficients in Table 1 were fitted based on a LS (Least Squares) approach in order to provide a unique path loss model. The best fit to the value of each coefficient was $PL(d_0) = 47.98$ dB, $\alpha = 3.467$ and $\sigma = 4.7$ dB, i.e., the combined path loss model is given by

$$PL(d_m)[\text{dB}] = \underbrace{47.98}_{PL(d_0)} + 10 \cdot \underbrace{3.467}_{\alpha} \cdot \log_{10}\left(\frac{d_m}{d_0}\right), \quad 20 \text{ m} \leq d_m \leq 600 \text{ m}. \quad (5)$$

Figure 5 shows the equivalent path loss expressed by (5) and the path loss models proposed by [7].

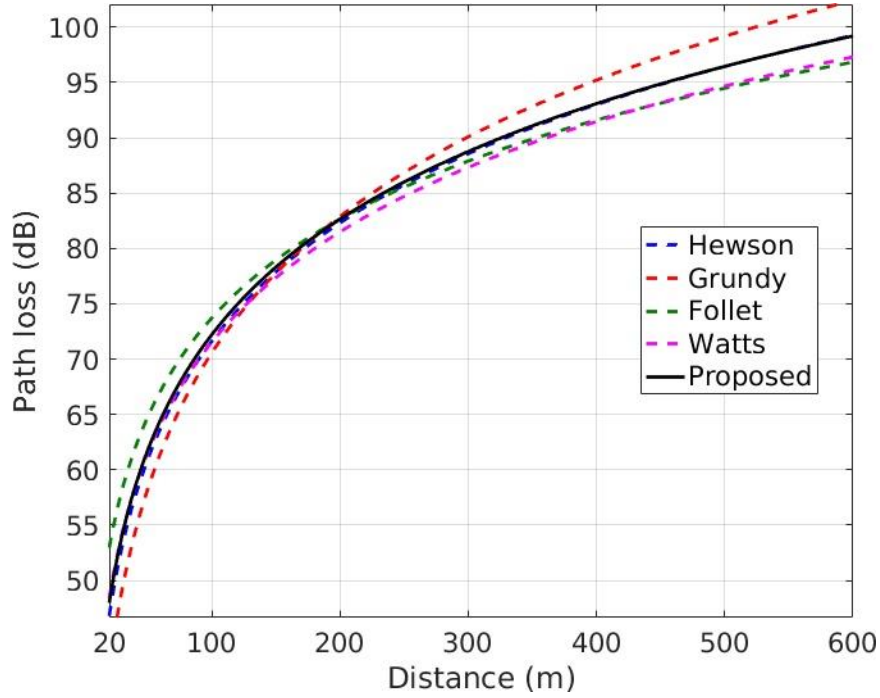


Figure 5. Path loss models proposed by [8] and equivalent/combined path loss model (black line).

- 2) The reference path loss $PL(d_0)$ in (5) was replaced by FSPL to become frequency dependent as follows

$$PL(d_0, f_{Hz})[\text{dB}] = G_t + G_r + 10 \cdot n \cdot \log_{10} \left(\frac{4\pi}{c} \cdot d_0 \cdot f_{Hz} \right), \quad (6)$$

where $G_t = G_r = -10.2$ dBi are the antenna gains of the transmitter and receiver from [7], respectively, c is the light speed in m/s and n is the attenuation coefficient which was adjusted to be equal to 2.3679 in order to fulfil the equality (6) when $f_{Hz} = 922 \cdot 10^6$ Hz. Reorganizing (6), the following result was obtained

$$PL(d_0, f_{MHz})[\text{dB}] = -22.22 + 23.679 \cdot \log_{10}(f_{MHz}), \quad (7)$$

which is the frequency dependent reference path loss. In order to remove the gap between the distances of the general case (1 km up to 50 km) and the D2D (20 m up to 600 m), the proposed path loss for the D2D, frequency dependent, is extended to 1 km, and it is given by replacing the reference path loss $PL(d_0)$ in (5) by (7), i.e.,

$$PL(d_m, f_{MHz})[\text{dB}] = -22.22 + 23.68 \cdot \log_{10}(f_{MHz}) + 34.67 \cdot \log_{10} \left(\frac{d_m}{d_0} \right). \quad (8)$$

Therefore, considering the scenarios analyzed in [7], for the 5G-RANGE project, in the D2D large scale parameters context, it is recommended the following parameters:

- Path loss model: Equation (8);
- Shadow standard deviation, $\sigma = 4.7$ dB.

For fast fading model, due to the small distances between Tx and Rx, the recommendations described in a previous section for the general case (i.e., DS, ASD, ASA, ZSD, and ZSA) cannot be applied for D2D communications. As such, for these parameters, for link and system level simulations, it is recommended to use CDL models from 3GPP TR 38.901 [2], scaled with the following values:

- DS = 500 ns [9];

- ASD = 9° [10];
- ASA = 55.3° [10];
- ZSD = 8° [10];
- ZSA = 18° [10].

2.2 Channel generation

The distribution of the small-scale fading parameters (angles and delays) is assumed not to change as a function of the distance between transmitter and receiver [6]. Under this assumption, the channel characterization for the fast fading described in [1] can also be used to characterize all the different links depicted in Figure 1.

The generation of the channel coefficients is almost the same as the one provided in [2], with a small difference proposed in [11]. The general channel impulse response is given by

$$H_{u,s,n,m}(t, \tau) = \sqrt{\frac{1}{k+1}} \cdot H_{u,s,n,m}^{\text{NLOS}}(t, \tau) + \sqrt{\frac{k}{k+1}} \cdot H_{u,s,0}^{\text{LOS}}(t), \quad (9)$$

where u is the antenna element index of the receiver, s is the antenna element index of the transmitter, n is the cluster index and m is the ray index within the cluster n . Also, k is the Rician k -factor in linear scale. In (9), $H_{u,s,n,m}^{\text{NLOS}}(t, \tau)$ is the channel impulse response due to the multipath components at time t and delay τ , and $H_{u,s,0}^{\text{LOS}}(t)$ is the channel coefficient due to the direct path between the receiver and transmitter (LOS case). In the NLOS case, the k -factor is equal to zero in the link Tx-Rx, and the channel impulse response in (9) is reduced to $H_{u,s,n,m}(t, \tau) = H_{u,s,n,m}^{\text{NLOS}}(t, \tau)$.

The coefficients $H_{u,s,n,m}^{\text{NLOS}}(t, \tau)$ and $H_{u,s,0}^{\text{LOS}}(t)$ in (9) are given by

$$H_{u,s,n,m}^{\text{NLOS}}(t, \tau) = \sqrt{\frac{P_n}{M}} \cdot \mathbf{f}_{\text{rx},u}^T \cdot \mathbf{X}_{n,m} \cdot \mathbf{f}_{\text{tx},s} \cdot d_{\text{tx},n,m} \cdot d_{\text{rx},n,m} \cdot \delta(\tau - \tau_{n,m}) \quad \text{and} \quad (10)$$

$$H_{u,s,0}^{\text{LOS}}(t) = \mathbf{f}_{\text{rx},u}^T \cdot \begin{bmatrix} 1 & 0 \\ 0 & -1 \end{bmatrix} \cdot \mathbf{f}_{\text{tx},s} \cdot \exp\left(-\frac{j2\pi \cdot d_{3D}}{\lambda}\right) \cdot d_{\text{tx},0} \cdot d_{\text{rx},0}, \quad (11)$$

respectively. The coefficients in (10) and (11) are described as follows:

- $\mathbf{f}_{\text{rx},u}$ and $\mathbf{f}_{\text{tx},s}$ are the antenna gains of the antenna elements u and s in the receiver and transmitter, respectively;
- $\mathbf{X}_{n,m}$ is the cross-polarization matrix of the ray m within the cluster n ;
- $d_{\text{rx},n,m}$ and $d_{\text{tx},n,m}$ are the Doppler effect of the ray m within the cluster n for the transmitter and receiver, respectively;
- $d_{\text{tx},0}$ and $d_{\text{rx},0}$ are the Doppler effect of the LOS ray (direct path) with the transmitter and receiver, respectively;
- P_n is the normalized power of cluster n ;
- M is the number of rays within each cluster;
- $\tau_{n,m}$ is the delay of the ray m within cluster n ;
- λ is the wave length $\lambda = \frac{c}{f}$ wherein $c = 3 \cdot 10^8$ m/s and f is the system frequency in Hz;
- d_{3D} is the 3D distance between the transmitter and receiver.

The coefficients $f_{rx,u}$, $f_{tx,s}$ and $X_{n,m}$ are given by

$$f_{rx,u} = \begin{bmatrix} F_{rx,u,\theta}(\theta_{n,m}^{ZOA}, \phi_{n,m}^{AOA}) \\ F_{rx,u,\phi}(\theta_{n,m}^{ZOA}, \phi_{n,m}^{AOA}) \end{bmatrix} \cdot \exp\left(\frac{j2\pi \hat{\mathbf{r}}_{rx,n,m}^T \cdot \bar{\mathbf{d}}_{rx,u}}{\lambda}\right), \quad (12)$$

$$f_{tx,s} = \begin{bmatrix} F_{tx,s,\theta}(\theta_{n,m}^{ZOD}, \phi_{n,m}^{AOD}) \\ F_{tx,s,\phi}(\theta_{n,m}^{ZOD}, \phi_{n,m}^{AOD}) \end{bmatrix} \cdot \exp\left(\frac{j2\pi \hat{\mathbf{r}}_{tx,n,m}^T \cdot \bar{\mathbf{d}}_{tx,s}}{\lambda}\right), \text{ and} \quad (13)$$

$$X_{n,m} = \begin{bmatrix} \exp(j\Phi_{n,m}^{\theta\theta}) & \sqrt{\omega_{n,m}^{-1}} \cdot \exp(j\Phi_{n,m}^{\theta\phi}) \\ \sqrt{\omega_{n,m}^{-1}} \cdot \exp(j\Phi_{n,m}^{\phi\theta}) & \exp(j\Phi_{n,m}^{\phi\phi}) \end{bmatrix}, \quad (14)$$

respectively. In (12), $F_{rx,u,\theta}$ and $F_{rx,u,\phi}$ are the field patterns of the receiver antenna element u to the pair of angles $(\theta_{n,m}^{ZOA}, \phi_{n,m}^{AOA})$ in the direction of spherical basis vectors $\hat{\theta}$ and $\hat{\phi}$, respectively, while $\hat{\mathbf{r}}_{rx,n,m}$ is the unit vector that represents the wave front of each ray m within a cluster n at the receiver and is given by

$$\hat{\mathbf{r}}_{rx,n,m} = \begin{bmatrix} \sin(\theta_{n,m}^{ZOA}) \cdot \cos(\phi_{n,m}^{AOA}) \\ \sin(\theta_{n,m}^{ZOA}) \cdot \sin(\phi_{n,m}^{AOA}) \\ \cos(\theta_{n,m}^{ZOA}) \end{bmatrix}. \quad (15)$$

The vector $\bar{\mathbf{d}}_{rx,u}$ in (12) is the relative position of the antenna element s and the coordinate of the antenna array of the receiver, i.e., $\bar{\mathbf{d}}_{rx,u}$ is a vector that points from reference coordinate of the antenna array to the antenna element. In the same manner, the coefficients $F_{tx,s,\theta}$, $F_{tx,s,\phi}$, $\hat{\mathbf{r}}_{tx,n,m}$ and $\bar{\mathbf{d}}_{tx,s}$ in (13) are defined in the same way as the ones in (12), but with respect to the transmitter. $\hat{\mathbf{r}}_{tx,n,m}$ is given by

$$\hat{\mathbf{r}}_{tx,n,m} = \begin{bmatrix} \sin(\theta_{n,m}^{ZOD}) \cdot \cos(\phi_{n,m}^{AOD}) \\ \sin(\theta_{n,m}^{ZOD}) \cdot \sin(\phi_{n,m}^{AOD}) \\ \cos(\theta_{n,m}^{ZOD}) \end{bmatrix}. \quad (16)$$

The Doppler effect of the ray m within the cluster n for the receiver and transmitter is given by

$$d_{rx,n,m} = \exp\left(\frac{j2\pi \hat{\mathbf{r}}_{rx,n,m}^T \cdot \bar{\mathbf{v}}_{rx}}{\lambda}\right) \quad (17)$$

and, in order to also consider D2D communications, there is an additional channel coefficient that considers the Doppler effect of the transmitter, given by

$$d_{tx,n,m} = \exp\left(\frac{j2\pi \hat{\mathbf{r}}_{tx,n,m}^T \cdot \bar{\mathbf{v}}_{tx}}{\lambda}\right), \quad (18)$$

wherein $\bar{\mathbf{v}}_{rx}$ and $\bar{\mathbf{v}}_{tx}$ are the speed of receiver and transmitter in Cartesian coordinate. In case of a fixed transmitter, such as a BS, (18) is equal to one.

In (14), the angles $\Phi_{n,m}^{\theta\theta}$, $\Phi_{n,m}^{\phi\theta}$, $\Phi_{n,m}^{\theta\phi}$ and $\Phi_{n,m}^{\phi\phi}$ are the initial phases for the ray m of each cluster n for four different polarization combinations $\theta\theta$, $\phi\theta$, $\theta\phi$ and $\phi\phi$. The distribution for initial phases is uniform in the interval $(-180^\circ, 180^\circ)$. $\omega_{n,m}$ represents the cross-polarization power ratio (XPR) which follows a log-normal distribution and is modelled independently for each ray within the cluster.

For link-level simulations and simple system-level modelling, the channel impulse response in (9) can be implemented using the CDL models from [2]. Taking into account the different links described in Figure 1, it is recommended to use the models CDL-A (NLOS) and CDL-D (LOS) presented in Annex B (general case) and Annex C (D2D) to characterize the channel model. In order to identify which CDL model should be used for a given link, the d_1/d_2 LOS probability model is recommended:

$$P_{\text{LOS}}(d) = \min\left\{\frac{d_1}{d}, 1\right\} \cdot \left[1 - \exp\left(-\frac{d}{d_2}\right)\right] + \exp\left(-\frac{d}{d_2}\right), \quad (19)$$

where d is the 2D horizontal distance between the transmitter and receiver, d_1 is the distance for which $d \leq d_1$ gives $P_{\text{LOS}}(d) = 1$ and d_2 is the distance that quantifies how fast the LOS probability decreases over the distance. The distances d , d_1 , and d_2 are defined in the same unit (meters or km).

The values of d_1 and d_2 can be different for each of the links presented in Figure 1. Moreover, such values may vary as a function of the scenario, e.g., plane terrain and hilly terrain.

Considering the recommendation of the values for the angular and delay already presented in this section, the angles and delays of the models CDL-A and CDL-D given in [2] were scaled using the equations in Annex A and are given in Table 11 and Table 12 for the general case (Annex B), or Table 13 and Table 14 for D2D (Annex C).

In the following, the steps to generate the channel coefficients in (9) are described.

1. Select one of the CDL models according to the considered use case, as follows:
 - General case:
 - Table 11 (NLOS);
 - Table 12 (LOS).
 - D2D:
 - Table 13 (NLOS);
 - Table 14 (LOS).
2. Generate the angles AOA, AOD, ZOA and ZOD in (12) and (13) for each ray $m \in \{1, 2, \dots, M\}$ within a cluster $n \in \{1, 2, \dots, N\}$ as follows

$$\phi_{n,m}^{\text{AOD}} = \phi_n^{\text{AOD}} + \phi_{\text{LOS}}^{\text{AOD}} + c_{\text{ASD}} \cdot \alpha_m^{\text{AOD}}, \quad (20)$$

$$\phi_{n,m}^{\text{AOA}} = \phi_n^{\text{AOA}} + \phi_{\text{LOS}}^{\text{AOA}} + c_{\text{ZSA}} \cdot \alpha_m^{\text{AOA}}, \quad (21)$$

$$\theta_{n,m}^{\text{ZOD}} = \theta_n^{\text{ZOD}} + \theta_{\text{LOS}}^{\text{ZOD}} + c_{\text{ZSD}} \cdot \alpha_m^{\text{ZOD}}, \quad (22)$$

$$\theta_{n,m}^{\text{ZOA}} = \theta_n^{\text{ZOA}} + \theta_{\text{LOS}}^{\text{ZOA}} + c_{\text{ZSA}} \cdot \alpha_m^{\text{ZOA}}, \quad (23)$$

where

- ϕ_n^{AOD} and ϕ_n^{AOA} are the angles AOD and AOA of cluster n from the selected CDL model;
- θ_n^{ZOD} and θ_n^{ZOA} are the angles ZOD and ZOA of the cluster n from the selected CDL model;
- $\phi_{\text{LOS}}^{\text{AOD}}$ and $\phi_{\text{LOS}}^{\text{AOA}}$ are the angles AOD and AOA which are calculated from the direct path between the transmitter and receiver;
- $\theta_{\text{LOS}}^{\text{ZOD}}$ and $\theta_{\text{LOS}}^{\text{ZOA}}$ are the angles ZOD and ZOA which are calculated from the direct path between the transmitter and receiver;
- c_{ASD} and c_{ASA} are the cluster azimuth spread of departure and arrival, respectively, from the selected CDL model;
- c_{ZSD} and c_{ZSA} are the cluster zenith spread of departure and arrival, respectively, from the selected CDL model;
- α_m is the angular offset which is applied to each ray within a cluster according to Table 2.

Table 2. Offset to each ray within a cluster.

Ray number m	1, 2	3, 4	5, 6	7, 8	9, 10	11, 12	13, 14	15, 16	17, 18	19, 20
Offset α_m	± 0.0447	± 0.1413	± 0.2492	± 0.3715	± 0.5129	± 0.6797	± 0.8844	± 1.1481	± 1.5195	± 2.1551

Note that the power of each cluster in the selected CDL model must be transformed to linear scale and normalized such that the sum of the power of all clusters has to be equal to one. Afterwards, these powers can be used in (10) to generate the channel coefficients. Moreover, note that the power of each ray within a cluster is given by $\frac{P_n}{M}$ as shown in (10), i.e., all the rays within a cluster have the same power.

3. Perform a random coupling of rays within each cluster for both azimuth and zenith, i.e., couple randomly the angles AOD ($\phi_{n,m}^{\text{AOD}}$) with AOA ($\phi_{n,m}^{\text{AOA}}$) and the angles ZOD ($\theta_{n,m}^{\text{ZOD}}$) with ZOA ($\theta_{n,m}^{\text{ZOA}}$).
4. Generate the XPR and the initial phases in (14) for each ray within a cluster. The XPR is given by

$$\omega_{n,m} = 10^{\frac{\Omega}{10}}, \quad (24)$$

where Ω is normal distributed with zero-mean and standard deviation σ_{XPR} given by the selected CDL model and the initial phases are uniformly distributed in the range $(-180^\circ, 180^\circ)$.

5. Calculate the path gain (p_g) and the shadowing (s_f), both in linear scale as follows

$$p_g = \left(10^{\frac{PL}{10}}\right)^{-1}, \quad (25)$$

and

$$s_f = 10^{\frac{SF}{10}}, \quad (26)$$

where PL and SF are the path loss and shadowing in dB.

6. Generate the channel coefficients $\tilde{H}_{u,s,n,m}(t, \tau)$ by combining the path gain in (25) and the shadow fading in (26) with the fast fading in (9), i.e.,

$$\tilde{H}_{u,s,n,m}(t, \tau) = \sqrt{p_g} \cdot \sqrt{s_f} \cdot H_{u,s,n,m}(t, \tau). \quad (27)$$

Note that, after this procedure and according to 3GPP TR 38.901 [2], clusters with power less than -25 dB can be removed.

2.3 Simulations Results

In this section, simulations regarding the path loss validation and channel capacity are presented. The simulation parameters are depicted in Table 3.

Table 3. Simulation parameters.

Parameter	Value	Unit
Cell radius	50	km
BS transmit power	49 and 53	dBm

Channel bandwidth	23.40	MHz
PRB (physical resource block) bandwidth	180	kHz
UE speed	3 and 120	km/h
Carrier frequency	700	MHz
Path loss model	FSPL + 29.38	dB
Shadowing std.	4.47	dB
Antenna configuration	1x1, 2x2, 4x4	-
Rad. power pattern for BS and UE	Isotropic	-
Antenna gain for {BS, UE, CPE}	{9, 0, 9}	dBi
Polarization for BS and UE/CPE	Vertical	°
Noise figure	5	dB
Noise power per PRB	-116.45	dBm
Number of UEs	1	-
Monte Carlo runs	5000	-

To analyze the capacity of MIMO channels, the CDF of the throughput was computed considering SISO (Single-Input Single-Output) and MIMO (2x2 and 4x4) configurations, with the UE placed at the cell-edge. The throughput is in fact the raw throughput that was calculated using the Shannon formula, without coding and not considering the efficiency of frame structure, as follows

$$r_{\text{SISO}} = \sum_{k=1}^{N_{\text{PRB}}} B \log_2(1 + \text{SNR}_k) \quad (28)$$

$$r_{\text{MIMO}} = \sum_{k=1}^{N_{\text{PRB}}} B \log_2 \left(\det \left[\mathbf{I} + \frac{\eta}{\gamma^2} \mathbf{H}_k \mathbf{H}_k^H \right] \right) \quad (29)$$

where B is the PRB bandwidth, \mathbf{H} is the channel matrix with dimension $N_{\text{UE}} \times N_{\text{BS}}$, $\eta = \frac{P_{\text{BS}}}{N_{\text{PRB}} N_{\text{BS}}}$.

The first validation is depicted in Figure 6, where the CDF of the proposed path loss model is compared with the CDF of the measurement data with and without outliers. As it can be observed, there is a good match between the measurements and the proposed model.

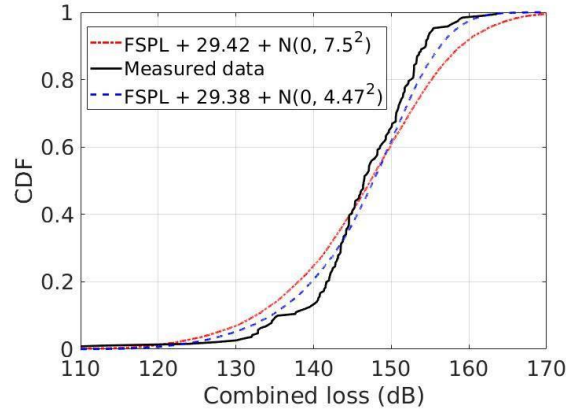


Figure 6. CDF of measured path loss in Figure 2.

From Figure 7 to Figure 10, the outliers were removed according to the criteria in [12].

In Figure 7, for a BS transmission power of 49 dBm, only MIMO configurations of the CPE achieve a transmission rate greater than 100 Mbps, averaged over time. While for the scenario in Figure 8, where the BS transmission power is 53 dBm, all configurations for CPE achieve an average throughput greater than 100 Mbps average of the time. It should be mentioned that the computed channel capacity is an upper bound for the actual channel capacity, since the Shannon formula was considered, i.e., in a real scenario the throughput should be less than the one presented. One way to overcome this issue is to use dual polarized antennas both at transmitter and receiver side. This scheme increases virtually the size of the array, which will increase the channel capacity. The curves in Figure 7 and Figure 8, show the throughput for a NLOS scenario. For comparison purposes, Figure 9 and Figure 10 consider the LOS scenario. A small gain can be observed for the LOS case over the NLOS case.

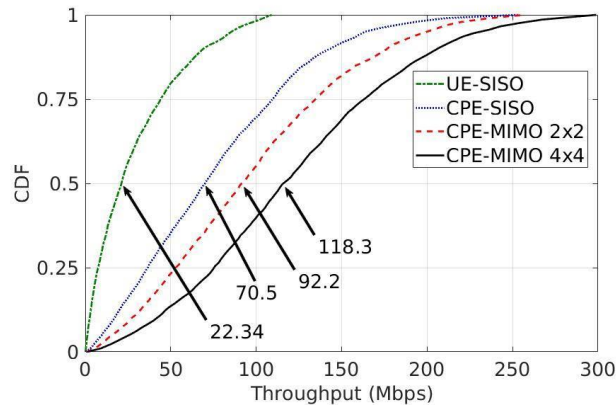


Figure 7. Channel Throughput for a Tx power of 49dBm, NLOS case.

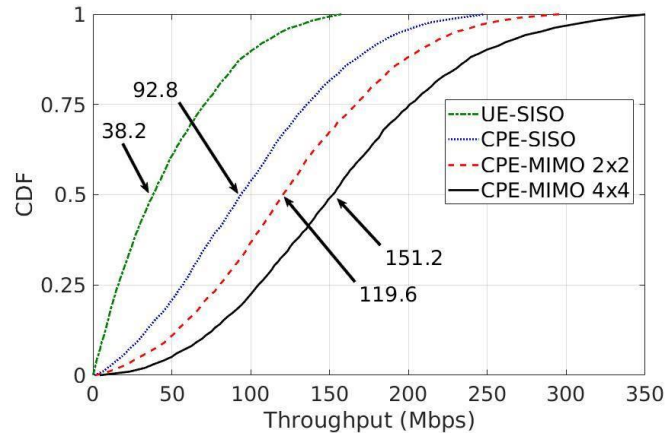


Figure 8. Channel Throughput for a Tx power of 53dBm, NLOS case.

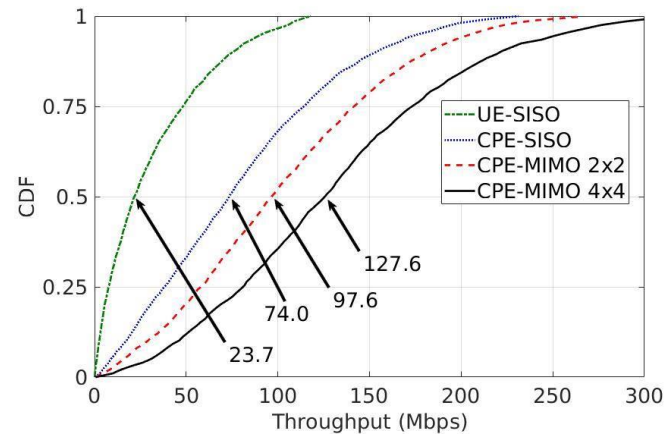


Figure 9. Channel Throughput for a Tx power of 49dBm, LOS case.

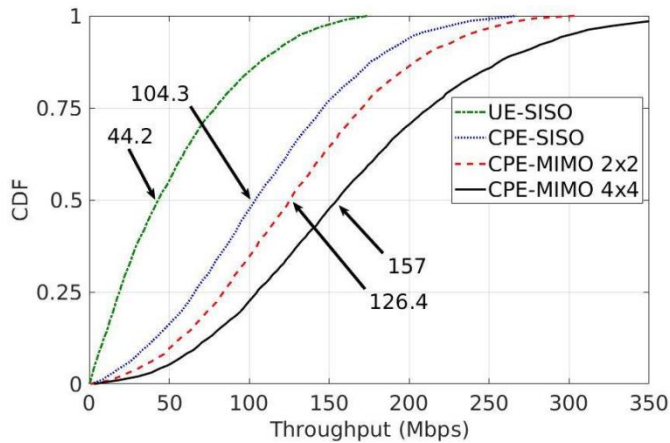


Figure 10. Channel Throughput for a Tx power of 53dBm, LOS case.

2.4 Delay profile characteristics of other channel models

As stated in Section 2.1, the channel models available in literature cannot be directly applied in the 5G-RANGE. The models developed and presented in Section 2.1 covers path loss, large and small-

scale fading as well as angular statistics. These models will be used in the 5G-RANGE project to calculate capacity, predict coverage, and as input to develop the PHY layer.

Most of the PHY layer parameters are chosen based on the statistical properties of the channel. As an example, the maximum subcarrier spacing, is derived from, the delay spread RMS. Although, the CP (cyclic prefix) duration, must be selected according to the absolute maximum excess delay, and not from the statistical parameters.

For this specific parameter, in order to cover the more severe propagation environment to be encountered in a deployment, the maximum excess delay proposed for Digital Television Broadcast, and the model developed by the IEEE 802.22 study group deserve special attention due to its similarity with the operation conditions to the 5G-RANGE specially the Brazil models that might be better aligned with the propagation environment where the PoC (Proof of Concept) will take place in Santa Rita, Brazil. Table 4 presents the maximum excess delay expected for these models [13] [14].

Table 4. Maximum excess delay of other channel models.

Model	Maximum Delay (μ s)
UK short delay	2.8
UK long delay	75
DVB-T (portable reception)	0.85
CRC	35
Brazil A	5.93
Brazil B	12.7
Brazil C	2.799
Brazil D	5.93
Brazil E	2.0
IEEE 802.22 (profile A)	21.0
IEEE 802.22 (profile B)	11.0
IEEE 802.22 (profile C)	33.0
IEEE 802.22 (profile D)	60.0

2.5 Discussions and Future Perspectives

Regarding to the channel characterization for the 5G-RANGE network, it has been proposed two different models for outdoor, based on measurements. The first one, denoted as the model for the general case, considers the links between 1 km and 50 km, while the second one is proposed for D2D communications, for distances between 20 m and 1 km. In Section 2.3, channel simulations were provided for the general case, in order to validate the path loss model. Also, since the project has the KPI (key performance indicator) of 100 Mbps at cell edge for a user (with no mobility, e.g., UE/CPE), the channel capacity using the Shannon formula with no coding was evaluated for different setups of BS transmission power, and it can be concluded that, in most cases for the CPE, the KPI is achieved (the exception was for 49 dBm of BS transmission power in a SISO case).

Remarking that these simulations provide theoretical upper bound values for the channel capacity, and the maximum array size is up to four antennas elements at the transmitter and/or receiver side, one possible solution to increase the channel capacity is to increase virtually the array size with dual-polarized antenna, e.g., a 4x4 MIMO configuration becomes a virtually 8x8 MIMO. Simulations including this feature is part of the 5G-MIMORA block that will be presented in the deliverable D3.2

“Physical Layer of the 5G-RANGE – Part: 2”, where part of the content will be reserved to discuss MIMO schemes techniques for the 5G-RANGE project.

3 5G-RANGE Waveforms

The 5G-FlexNOW (5G Flexible Non-Orthogonal Waveforms) is an innovative modulation block that will encompass the main waveforms considered for future mobile networks.

To fulfill the 5G-RANGE requirements [1], regarding operation in TVWS bands, is essential that the PHY allows fragmented spectrum exploitation. Multicarrier waveforms offer good flexibility in spectrum allocation and are adequate for the 5G-FlexNOW. Another important PHY characteristic is low OOB emissions, since the spectrum mobility is a key feature for the cognitive cycle.

The main goal of the next subsections is to briefly present the candidate waveforms for the 5G-FlexNOW block.

3.1 OFDM

OFDM (orthogonal frequency division multiplexing) is a waveform adopted by many wireless communications standards, mainly due to its robustness against multipath propagation and relative low implementation complexity using FFT (fast Fourier transform). OFDM is the waveform used in the 3GPP LTE, Mobile communication standard and by the 5G NR.

3.1.1 OFDM waveform description

Error! Reference source not found. depicts the block diagram of an OFDM modulator/demodulator chain. The OFDM modulator splits the stream of QAM (quadrature amplitude modulation) symbols in many streams, transmitted in parallel, modulating narrow subcarriers over the channel. In this way, the bandwidth occupied by every subcarrier is narrower than the channel coherence bandwidth. Therefore, flat fading per subcarrier can be assumed.

The frequency of the subcarriers is selected in such way that, despite overlapping, they are orthogonal to each other. This feature improves the spectrum efficiency when compared with frequency division multiplexing. In fact, for large number of subcarriers ($K \geq 64$) and short channel delay profile, the OFDM and single carrier spectrum efficiencies are equivalent. After the inverse FFT on the transmit side, a CP (cyclic prefix) is added for each OFDM symbol to protect the data against the time-dispersive channel. If the CP is larger than the channel delay profile, the channel becomes circulant, allowing for frequency domain equalization (FDE) to be used on the receive side.

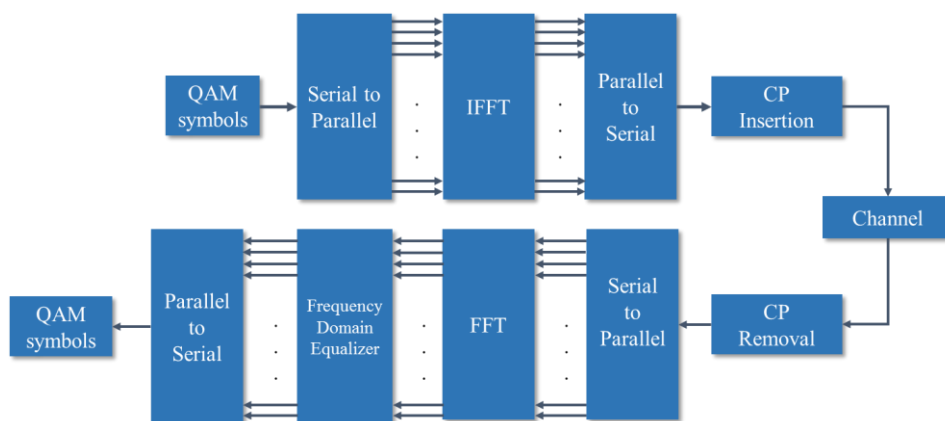


Figure 11. OFDM modulator and demodulator block diagram.

3.1.2 OFDM advantages and disadvantages

One advantage of OFDM over other multicarrier waveforms is that it is efficiently implemented in hardware or software using the FFT algorithm. This results in a low complexity transceiver chain in terms of signal processing. The use of CP allows for a simple equalization in the frequency-domain

after the OFDM demodulation (FFT). Robustness against multipath channel is achieved with low complexity and high spectrum efficiency, if the number of subcarriers is high and the channel delay profile is short.

However, OFDM has some drawbacks that might hinder its application in the remote area scenario. The first one is the high OOB emissions. In OFDM, the QAM symbols modulating every subcarrier change abruptly at every OFDM symbol creating a discontinuity. This operation is equivalent to modulate the subcarriers with rectangular pulse in time domain. In frequency domain, the rectangular pulse has bad-localized sinc-shaped spectrum, which leads to high OOB emissions, as shown in Figure 12.

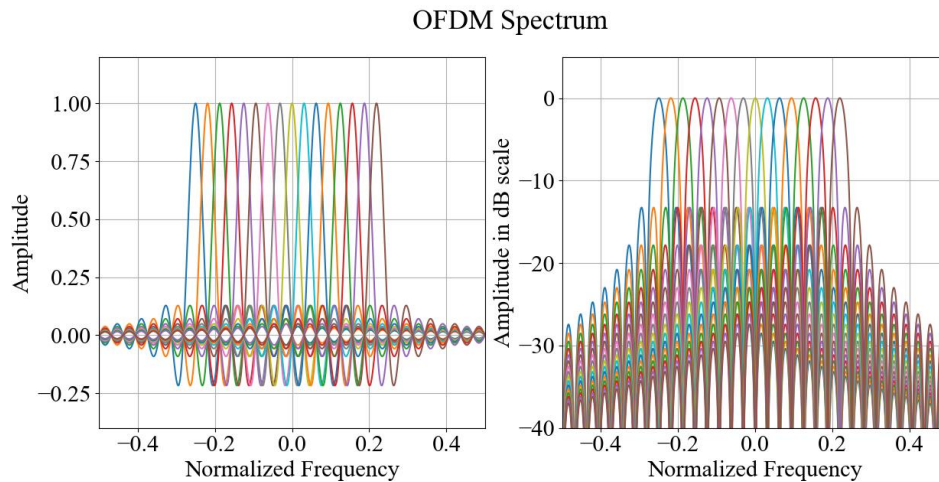


Figure 12. OFDM spectrum and its OOB emissions.

Another issue with OFDM is the CP efficiency when the channel delay profile is large. In this case, CP must be very long and its duration can represent a large parcel of the overall OFDM symbol duration. As the CP does not carry useful information, it leads to a poor spectral efficiency. Increasing the number of subcarriers also increases the OFDM symbol time and partially compensates the long CP length. However, this approach also increases the complexity and reduce the robustness against Doppler effect, hence this solution can be prohibitive for the core use cases (e.g., agribusiness and smart farming for remote areas) described in D2.1. **Error! Reference source not found.** shows the CP insertion and overhead associated.

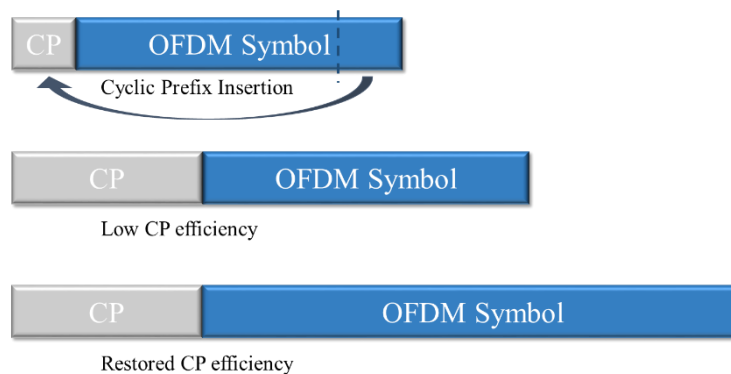


Figure 13. Cyclic prefix overhead in OFDM.

3.2 F-OFDM

The F-OFDM (filtered OFDM) waveform is a variation of the OFDM and have the same benefits. It is also a multi-carrier waveform robust to multipath propagation and employs a CP to avoid ISI. This

section will describe this waveform highlighting its main characteristics including advantages and disadvantages when compared to the other waveforms considered the 5G-RANGE PHY.

3.2.1 F-OFDM waveform description

The F-OFDM waveform introduces a subband filter to reduce the out-of-band emissions. In this waveform, the length of the filter impulse response is comparable to the OFDM symbol and not limited by the CP length. This allows narrow filters with sharp transition between passband and stopband, in such way that, it is possible to filter small groups of subcarriers, or resource blocks individually [15]. The long filter leads to ICI (inter-carrier interference) and ISI (inter-symbol interference) but proper filter design keeps these interferences at acceptable levels. Figure 14. F-OFDM downlink block diagram. depicts the F-OFDM block diagram for the downlink showing the filters.

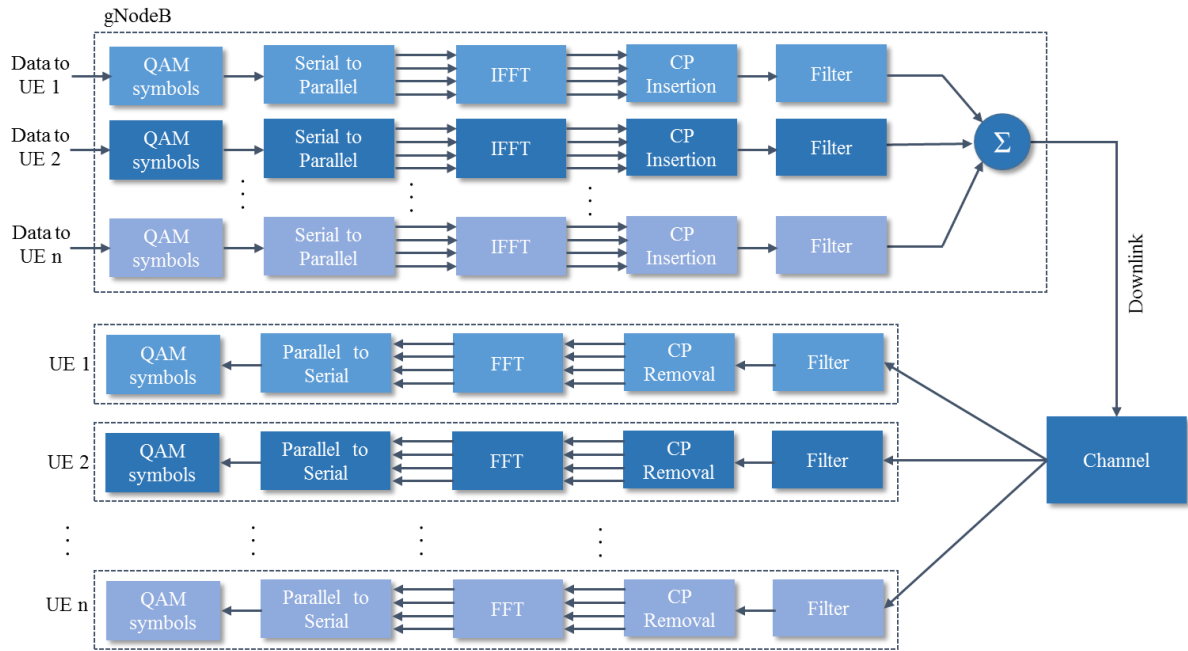


Figure 14. F-OFDM downlink block diagram.

3.2.2 F-OFDM advantages and disadvantages

The ability to filter a group of subcarriers allows different subcarrier spacing, and symbol time durations, also referred as numerology, to coexist at the same time in the downlink. Even not being orthogonal to each other, the filter removes the OOB emissions from each group of subcarriers and reduces the interference among subbands. For further inter subband interference reduction, it is possible to turn off subcarriers as guard band. On the uplink direction, in addition to support many numerologies, the F-OFDM waveform also allows different asynchronous users to share the spectrum without interfering on each other, if a guard band is used. Figure 15 depicts the F-OFDM spectrum.

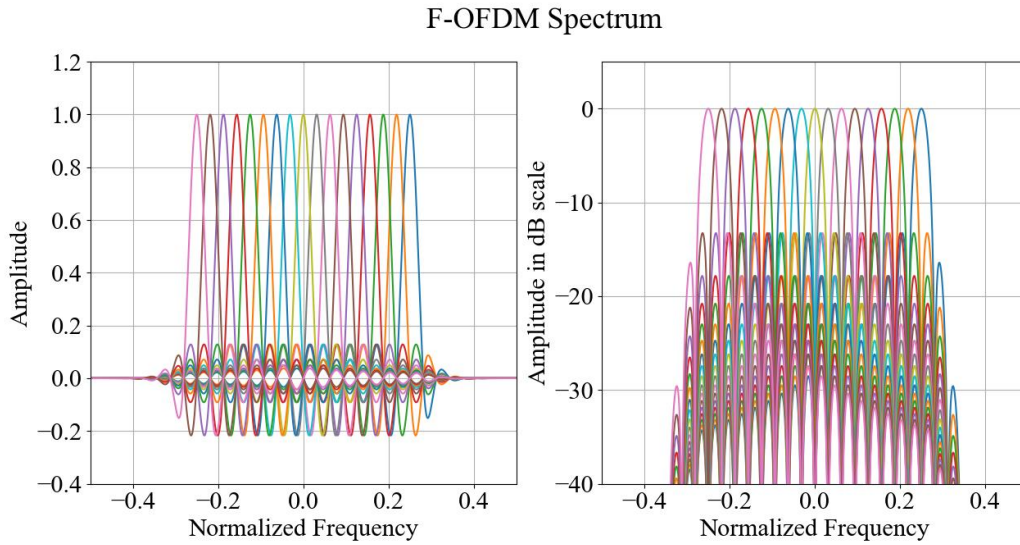


Figure 15. F-OFDM spectrum with reduced OOB emissions.

The main disadvantage of the F-OFDM approach is the complexity added by the filter operation in both directions. At the gNB (next generation eNodeB), a filter bank is applied to groups of subcarriers assigned to different numerologies. The UE applies the filter in both directions reducing the OOB emissions of the group of subcarriers allocated to the UE transmission, and rejecting OOB emission from subcarriers allocated to other users in the reception.

3.3 GFDM

The use cases and requirements described in D2.1 show that the 5G-RANGE network needs a flexible waveform. GFDM (generalized frequency division multiplexing) [16] is a new waveform that adds another dimension to the transmitted signal by arranging the data symbols both in time and frequency domains. Hence, many narrow subcarriers can be used to increase performance in a very frequency-selective channel or a small number of subcarriers and a large number of subsymbols can be employed to reduce the signal PAPR. Each subcarrier is individually filtered, and a single CP can protect multiple subsymbols, resulting in low OOB emissions and high spectrum efficiency. This section will present the main characteristics of this innovative waveform.

3.3.1 GFDM Waveform Description

GFDM is a non-orthogonal multicarrier waveform that employs different versions of a prototype pulse, each one circularly shifted both in time and frequency domains and scaled by a corresponding QAM data symbol. In this sense, user information is arranged in K subcarriers by M subsymbols time-frequency grid, yielding to $N=MK$ data symbols to be transmitted in a GFDM block. Just one CP is added to protect the entire block, i.e., a single CP protects M subsymbols.

The format of the transmission pulse and the active sub-symbols of the grid allows for controlling the characteristics of the PSD (power spectrum density) and OOB emission [17]. The design of the receiver pulse of the linear demodulator allows for achieving a specific goal, such as self-interference cancellation with the ZF (zero forcing) approach and SNR maximization with MF (matched filter). The MMSE can perform as MF for low SNR (signal to noise ratio) and ZF for high SNR, at the cost of a higher complexity. Figure 16 depicts the block diagram of a GFDM modulator/demodulator chain.

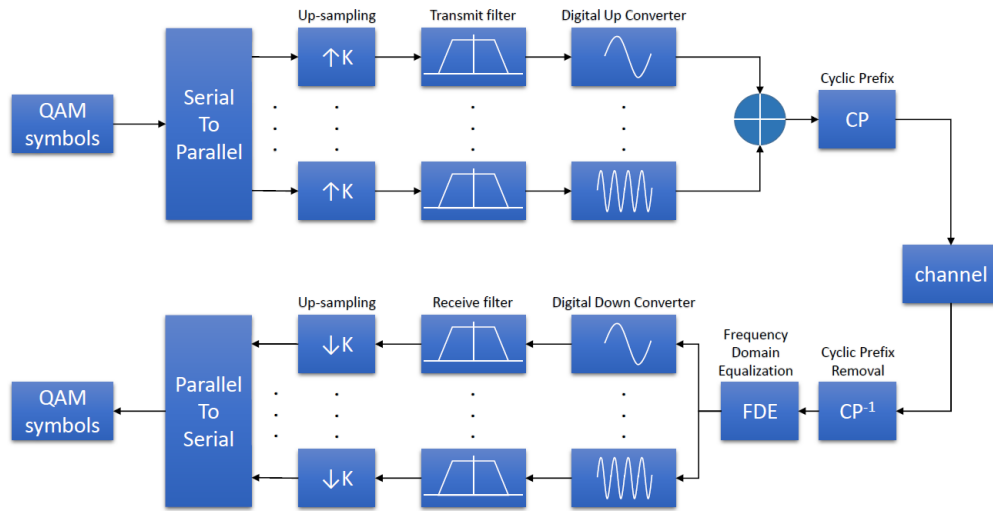


Figure 16. GFDM modulator and demodulator block diagram.

The GFDM uses CP more efficiently when compared with other OFDM based waveforms. While OFDM uses one CP to protect K data symbols from the multipath channel, the same CP protects KM data symbols carried by the GFDM block. Figure 17 depicts the GFDM block as a time-frequency grid with K sub-carriers and M sub-symbols.

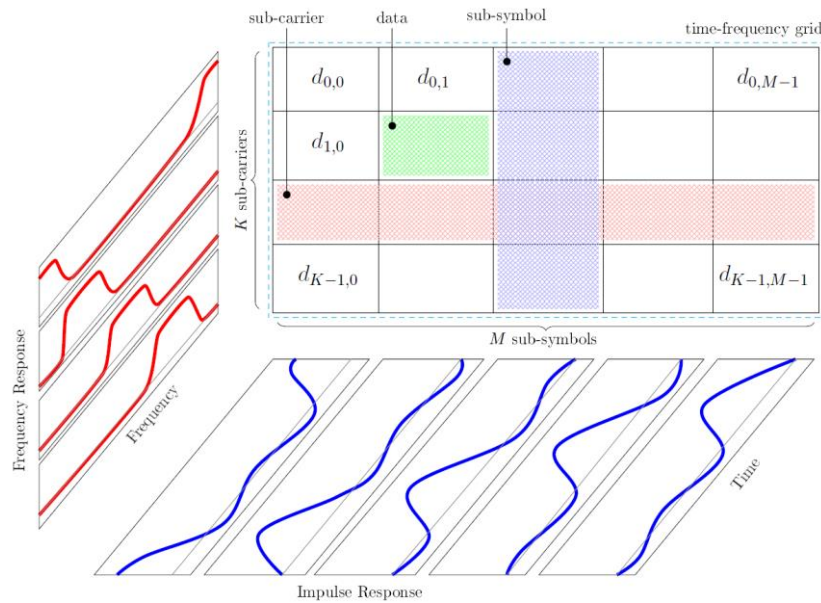


Figure 17. GFDM symbol structure as a time-frequency grid.

3.3.2 GFDM advantages and disadvantages

Besides OOB emission control and better CP efficiency, the ability to choose the parameters M , K and the prototype pulse also grants great flexibility to GFDM. As examples, setting $M=1$, $K=N$ and employing a rectangular pulse leads to the OFDM waveform. Using the configuration $K=1$, $M=N$ and a Dirichlet pulse yields the SC-FDE (single-carrier frequency domain equalization) waveform [18].

Figure 18 compares the OOB emission of OFDM and GFDM with $K=128$ and 75 active subcarriers. GFDM employs $M=7$ active subsymbols and RC (raised cosine) filter with roll-off factor of 0.5. The GFDM waveform presents a lower OOB emission than OFDM.

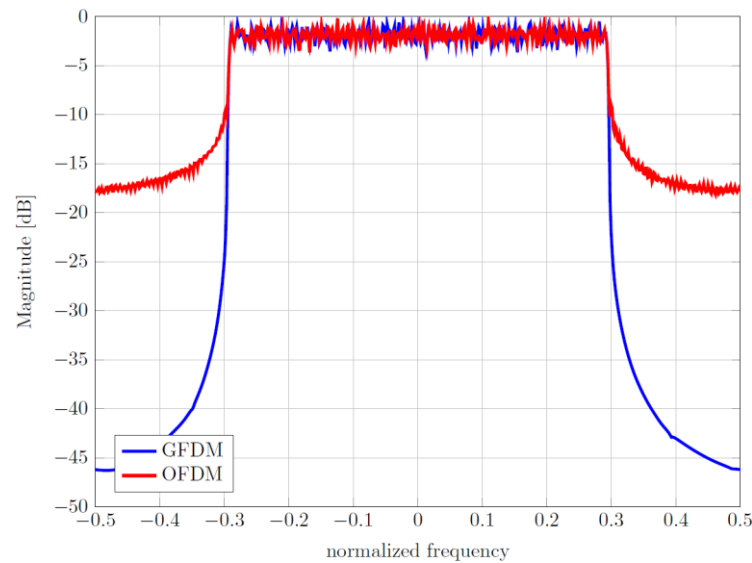


Figure 18. PSD comparison of OFDM and GFDM.

The block structure of GFDM allows for applying space-time coding to harvest diversity gain [19] or multiplexing gain [20]. The implementation complexity for diversity gain achieving space-time codes is low and similar for orthogonal and non-orthogonal waveforms. However, implementing multiplexing with non-orthogonal waveforms like GFDM usually results in a very high complexity.

The principal disadvantage of GFDM when compared with OFDM lies on the moderate increase of implementation complexity [21]. Another aspect is the increased latency when the number of sub-carriers of GFDM and OFDM are equal and the number of sub-symbols is greater than one. In this case, the latency to demodulate each sub-symbol is M times greater than OFDM.

3.4 B-OFDM

B-OFDM (block OFDM) is a straightforward extension of OFDM that can be used to improve the CP efficiency. The main principle is like GFDM, where several symbols are protected by a single CP. However, in this case, no filtering is employed. This section will present its main characteristics.

3.4.1 B-OFDM Waveform Description

B-OFDM is an OFDM based waveform that employs a single initial CP for several OFDM symbols as shown by Figure 19.

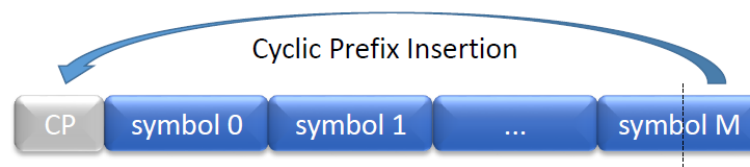


Figure 19. B-OFDM block structure.

This approach allows B-OFDM to achieve a high CP efficiency, especially when the symbol duration is short and the channel delay profile is long. Figure 20 illustrates the modulator and demodulator block diagram of B-OFDM.

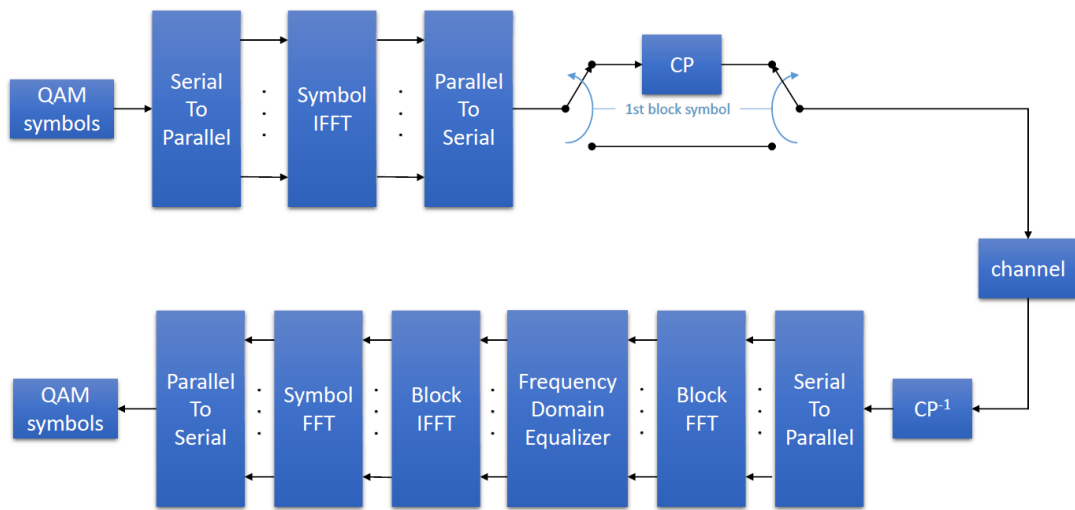


Figure 20. B-OFDM modulator and demodulator block diagram, where the CP insertion should be understood as prepending a copy of the end of the last OFDM symbol in the block before the first OFDM symbol, as depicted in Figure 19.

The single initial CP corresponds to the final samples from the last symbol of the block copied just before the first symbol, protecting the entire block of OFDM symbols from the dispersive characteristic of the transmission channel. This approach yields in a circular convolution of the transmitted block and the channel impulse response, allowing for a FDE with the block length to remove ICI and ISI prior to regular OFDM demodulation.

3.4.2 B-OFDM advantages and disadvantages

The principal advantage of B-OFDM is the possibility to increase the CP efficiency when the channel impulse response is long, concatenating several OFDM symbols and adding a single initial CP.

The major drawback of this approach is the increase of latency as it is necessary to equalize the entire block prior to demodulation of each symbol. For use cases that are insensitive to latency (e.g., data connectivity over long distances for remote areas), the only remaining drawback is the increment of complexity due to FDE (frequency domain equalizer) of the entire block.

3.5 Discussion and Future Perspectives

The waveforms presented in this section are considered the most suitable for the 5G-RANGE PHY. OFDM is used in many communications standards, including 4G and 5G communications, and it is robust to severe multipath channels, as is the case for 5G-RANGE. In channels with long excess delay spread, the CP used in OFDM can have a significant impact on the efficiency. To overcome that GFDM and B-OFDM are options that achieve higher efficiency by reducing the associated overhead. Opportunistic spectrum usage, as proposed in 5G-RANGE, requires low OOB emissions. F-OFDM and GFDM can naturally offer those advantages. OFDM and B-OFDM have higher OOB emissions, but windowing [16] can be applied to those waveforms in order to reduce these emissions to acceptable levels.

GFDM was one of the waveforms studied by the 5GNOW (5th Generation Non-Orthogonal Waveforms for Asynchronous Signaling) project along with UPMC (Universal Filtered Multi-Carrier), FBMC (Filter Bank Multi-Carrier) and BFDM (Biorthogonal Frequency Division Multiplexing). Despite the fact of the focus of the 5GNOW project was on the aspect of relaxed synchronization [22], GFDM waveform, as stated in Section 3.3, also exhibits low OOB and offers good CP efficiency, which are required characteristics for operation on TVWS and channels with long delay spread. A comparative study showed that GFDM has better overall performance when compared with the other 5G candidates [23].

In the next steps of the project, the performance of the proposed waveforms will be evaluated, under the channel models presented in Section 2 of this report, and the most suitable waveform for the core use cases presented in D2.1 will be identified.

4 Channel coding for 5G-ACRA

This section investigates FEC (forward error correction) schemes for the application in 5G-ACRA (5G advanced coding for remote areas). The 5G-RANGE target scenario with its long-range channel, as investigated in section 2, is expected to result in severe signal distortions, making reliable communication challenging. Furthermore, for the economic success of the proposed communication system a low power consumption as well as a low implementation complexity are important to reduce costs. As a result, the chosen FEC scheme for 5G-ACRA should on the one hand be extremely powerful to enable reliable transmission through the considered channel. On the other hand, the encoding and decoding complexity should be as low as possible to enable affordable end-user devices with low power consumption.

5G-ACRA will be implemented within the PHY (physical layer) of each 5G-RANGE compatible transceiver. The main purpose of this block is to implement bit interleaving (de-interleaving) of the incoming payload bits, encoding (decoding) of the interleaved bits and subsequent rate matching (rate recovery) in the transmission (reception) mode of the transceiver. The operation of this block is specified by the parameters in Table 5. The block size B and code rate R are flexibly determined in the MAC layer by the 5G-LA (5G Link Adaption). Note that in Table 5 block size and code rate are the only necessary parameters; all other parameters are optional.

Table 5. 5G-ACRA specifications.

Parameter	Value
Block size B	Length of the code words, which are the output of 5G-ACRA encoding
Code rate $R=D/B$	Ratio of number of information bits D to total number of bits per block B
FEC scheme (optional)	Choose FEC scheme if multiple schemes are supported
Interleaver type (optional)	Choose interleaver type if multiple interleavers are supported
En-/Decoding algorithm (optional)	Choose en-/decoding algorithm if multiple algorithms are supported
Max. iterations / list size (optional)	Specify max. number of iterations of the decoding algorithm / list size of the decoder to trade-off performance and complexity

The main channel coding scheme of 3GPP LTE (Long Term Evolution) is a Turbo code [24]. In the succeeding 3GPP NR (new radio) a Polar and a LDPC (low-density parity-check) code are used for FEC on the control and transport channels, respectively [25]. Table 6 Table 6 provides an overview on which channel coding scheme is applied on which channel in 5G NR. We will use these three previously introduced channel coding schemes as a starting point to find a suitable scheme for the application in 5G-ACRA. The remainder of this section is organized as follows: First, we will introduce Turbo, LDPC and Polar codes, and then we will compare them in terms of FEC performance and implementation complexity. This section will be concluded by a discussion of the results.

Table 6. Overview on the channel coding schemes for 5G NR channels [25]. The uplink and downlink control information channels are denoted by UCI and DCI, respectively. UL-SCH and DL-SCH denote the uplink and downlink shared channels and PCH and BCH denote the paging channel and broadcast channel, respectively.

	Control Channel	Transport Channel
Uplink	UCI (Polar)	UL-SCH (LDPC)
Downlink	DCI (Polar/Block)	DL-SCH (LDPC)
		PCH (LDPC)
		BCH (Polar)

4.1 Turbo codes

The turbo code employed in LTE is based on convolutional codes [24] (for more information on convolutional codes see e.g. [26]). The basic idea is to concatenate two or more simple convolutional codes in parallel or serial to obtain a combined code, which is much stronger than the individual codes. **Error! Reference source not found.** gives an overview on the encoder, which is specified in LTE in [24]. The input stream c_k is fed directly into the first convolutional encoder and an interleaved version is fed into the second convolutional encoder in parallel. The encoded code word is obtained as the concatenated output from both convolutional encoders.

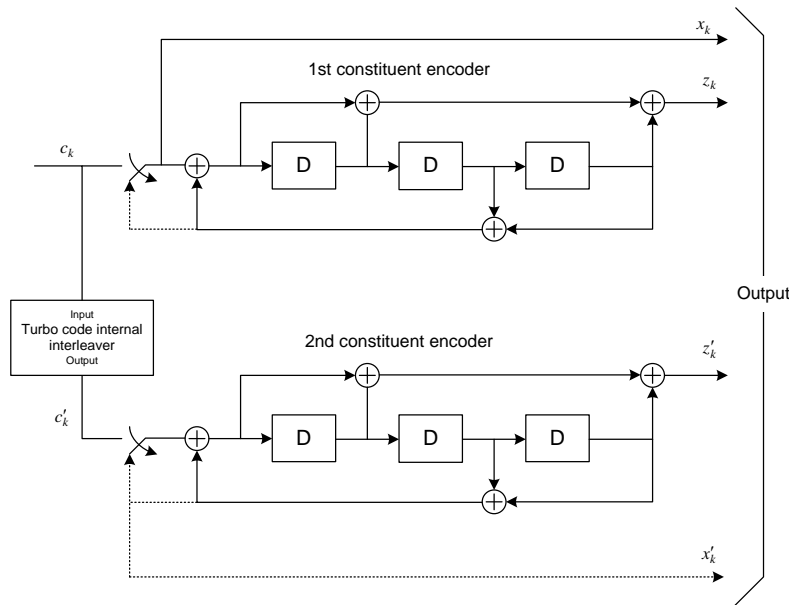


Figure 21. Structure of rate 1/3 Turbo encoder as specified in [24].

An example for a typical Turbo decoder is depicted in Figure 22. The decoder consists of two soft-output convolutional decoders, denoted as soft decoder 1 and 2 in Figure 22, an interleaver and a de-interleaver. The decoder starts e.g. by using the received soft input \mathbf{z} to compute a soft estimate $\hat{\mathbf{x}}_1$. This soft estimate is fed into the interleaver to convert it to an improved input $\tilde{\mathbf{x}}_2$ for the second soft decoder and produces another improved soft estimate, denoted as $\hat{\mathbf{x}}_2$. De-interleaving of $\hat{\mathbf{x}}_2$ yields $\tilde{\mathbf{x}}_1$.

which can be used as an improved input for the first soft decoder. This process can be repeated iteratively to obtain an iterative improvement of the estimated bits. The name *Turbo* code originates from similarities between the decoding algorithm and the feedback of exhaust gases in combustion engines in so-called *Turbo chargers*.

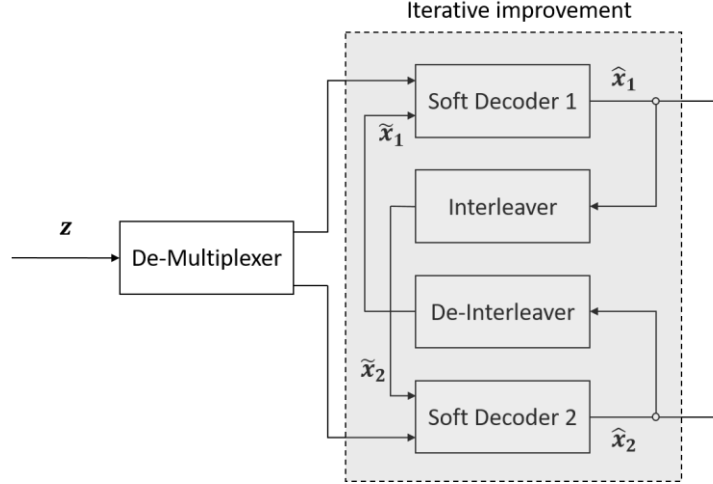


Figure 22: Principle of Turbo decoding.

4.2 LDPC codes

LDPC codes were first introduced by Gallager in 1963 [27] and they are used in many standards today. They are traditionally defined by a sparse parity check matrix \mathbf{H} , where sparse means that most elements of \mathbf{H} are “0”. In general, a parity check matrix has the property that for each valid code word \mathbf{c}_i it holds: $\mathbf{H}\mathbf{c}_i^T = \mathbf{0}^1$. The 5G NR LDPC code belongs to the class of QC-LDPC (quasi-cyclic LDPC) codes [28]. LDPC codes of this class are also used e.g., in IEEE 802.11n. QC-LDPC codes are defined as block matrices, where each block is either a matrix of all “0” elements or a circularly shifted version of the identity matrix. This definition allows memory efficient storage of the parity check matrix \mathbf{H} . This block definition of \mathbf{H} for QC-LDPC codes is sometimes denoted as protograph or BG (base graph). Defining a flexible BG has the advantage that the actual parity check matrix can be constructed in different sizes (corresponding to different code word block sizes B) from the same BG. This makes QC-LDPC codes highly flexible.

Table 7. Supported code rates and block sizes for 3GPP 5G NR base graph (BG) 1 and 2.

	BG1	BG2
Code rates R	1/3 – 8/9	1/5 – 2/3
Block sizes B	300 – 8448 bits	40 – 3840 bits

5G NR specifies a QC-LDPC code, which is used to protect the data on the transport channel and consists of two BGs [25]. Table 7 gives an overview on the supported code rates and block sizes for each BG. When to choose which BG is specified in [25], but in most practical situations, BG1 is used. The design of the two base graphs contains multiple special design features, which are introduced in the following.

¹ Here \mathbf{c}_i and $\mathbf{0}$ represent column vectors, where all elements of $\mathbf{0}$ are “0”.

Figure 23 provides a simplified overview on the parity check matrix structure of the 5G NR LDPC code. The columns can be separated into three groups: information columns, which are related to the information bits, core parity columns, which contain the parity checks for the highest possible code rate, and extension parity columns, which are used to decrease the code rate by including additional parity checks. This allows to flexibly adopt the code rate by only using an upper-left submatrix of the full parity check matrix. This is graphically illustrated in Figure 23, where all-zero blocks are shown in white and non-zero blocks colored. By using the upper-left most part of the parity check matrix, which contains the core check rows and the information and core parity columns, a parity check matrix with a code rate of $R = 8/9$ is obtained (for BG1). Now the code rate can be reduced by diagonally increasing the size of the matrix, such that it includes one or more extension parity columns. If all extension parity columns are used, the resulting code has a code rate of $R = 1/3$, which corresponds to the lowest possible code rate (cf. Table 7).

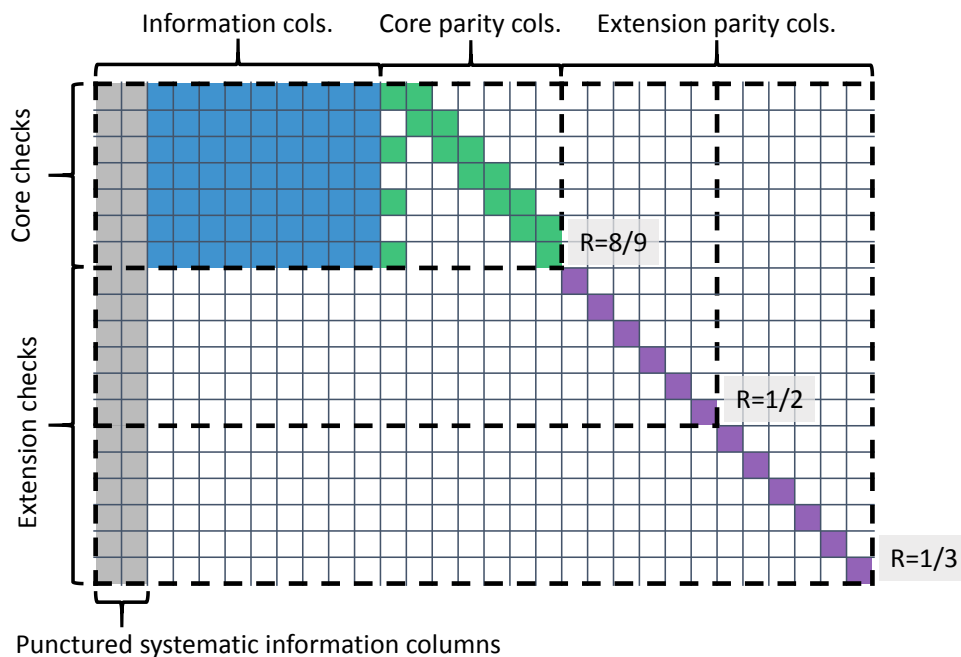


Figure 23. Simplified overview of the parity check matrix structure of the 5G NR base graphs.

This is a significant design improvement, because it allows to increase the throughput of the decoder for higher code rates as shown in [6]. In contrast, for Turbo codes the throughput is independent of the code rate. As a result, the design of the 5G NR LDPC codes makes it easier to achieve high data rates. Another benefit of this flexible structure is the support for IR-HARQ (incremental redundancy hybrid automatic repeat request), which essentially means to retransmit additional parity bits which may allow to successfully decode the code word instead of retransmitting the whole encoded code word [28], [29]. For more detailed information on IR-HARQ, the reader may refer to [30]. A further new design element is the puncturing of the first two information bit columns. The idea is to increase redundancy without reducing the code rate. In the 3GPP performance evaluation it has been shown that this approach increases the performance.

4.3 Polar codes

Polar codes were discovered recently by Arikan [31]. The data is encoded by a so-called *channel polarization* operation. Investigating the PoE (probability of error) of the individual output bits of a Polar decoder, the bits can be divided into two disjoint sets: for bits in the first set, the PoE is close to 0 and, for bits in the second set, the PoE is close to 1. This phenomenon is denoted as channel polarization. Intuitively, the idea for practical application is then to transmit the information bits on the

set of channels which have a PoE close to 0 and to transmit “0”-bits (so-called frozen bits) on the set of channels with PoE close to 1. The basic channel polarization operation for a block size of $B = 2$ is depicted in Figure 24. The first channel input x_1 is the binary XOR of the two input bits u_1 and u_2 . The second channel input is simply the second input bit $x_2 = u_2$. In this example, it can be shown that the PoE of u_2 is much lower, because it is effectively transmitted over both channels uses. By recursively applying the transformation, it is possible to construct arbitrary polar codes with any block size B that is a power of 2: $B = 2^k, k = \{1, 2, \dots\}$.

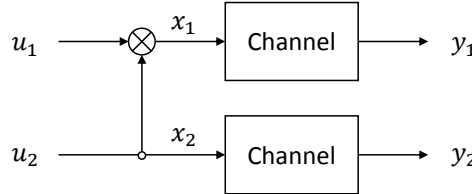


Figure 24. Channel polarization for $B = 2$.

Polar code decoding can straightforwardly be implemented by SC (successive cancellation) decoding [32], [33]. For the simple Polar code of Figure 24 with block size $B = 2$, the decoding algorithm is given by

$$(R1) \quad \hat{u}_1 = 2 \tanh^{-1} \left(\tanh \left(\frac{\tilde{y}_1}{2} \right) \tanh \frac{\tilde{y}_2}{2} \right)$$

$$(R2) \quad \hat{u}_2 = (-1)^{\hat{u}_1} \tilde{y}_1 + \tilde{y}_2,$$

where $\tilde{\mathbf{y}} = [\tilde{y}_1, \tilde{y}_2]^T$ denote realizations of received LLR (log-likelihood ratio) values (corresponding to soft information). As a more practical example, the given Polar code with $B = 2$ could be configured to a code rate of $R = 1/2$ by enforcing $u_1 = 0$ (in this case, u_1 is denoted as a frozen bit). Now the decoder obtains a soft estimate \hat{u}_2 of u_2 using the decoding rule (R2) as

$$\hat{u}_2 = (-1)^{\hat{u}_1} \tilde{y}_1 + \tilde{y}_2 = (-1)^0 \tilde{y}_1 + \tilde{y}_2 = \tilde{y}_1 + \tilde{y}_2.$$

In this configuration, the Polar code is identical to a repetition code of length $B = 2$ and the decoding rule above can be understood as averaging over the two noisy observations. A binary decoded code word is obtained by hard thresholding of the soft estimates. For decoding of Polar codes with a larger block size, the decoding rules (R1) and (R2) can be applied recursively (see [32], [33] for more information on SC decoding of Polar codes).

As mentioned before, 5G NR uses Polar codes for FEC mostly on the control channel [25]. However, the 5G NR Polar code is enhanced by appending a CRC check to the information bits. The resulting code is called a CA-Polar (CRC-aided Polar) code. The advantage is that the CRC can be used for SCL (successive cancellation list) decoding, where a list of code word candidates is kept and the CRC is used to determine a valid code word from the list of candidates for algorithm termination [34]. By using SCL decoding, the performance of Polar codes is on the same level as modern Turbo and LDPC codes.

4.4 Forward error correction performance

This subsection covers the performance analysis of the previously introduced channel coding schemes. The first part will introduce the simulation framework and the second part will compare the performance.

4.4.1 Simulation Framework

The performance of the channel coding is evaluated through simulations in *MATLAB*. The *MATLAB LTE Toolbox* provides an implementation² of the 3GPP LTE Turbo code as specified in [24]. Similarly, for the 5G NR Polar code there is an existing open-source *MATLAB* library³, which is compliant to [25] and which is developed by the University of Southampton, UK. This library supports SCL decoding with a flexible list and code block size. Therefore, it is well suited to be used in a performance comparison.

In contrast, there is no implementation of the 5G NR LDPC code available as specified in [25]. Therefore, within the project, a new *MATLAB* 5G NR LDPC library has been developed, which is publicly available on *GitHub*⁴. The implementation is compliant to the 3GPP 5G NR specifications in [25], however, it just supports a subset of the possible configuration so far. The decoder implements the SPA (sum-product-algorithm) according to [35]. The SPA is the optimal decoding algorithm in terms of performance and hence well suited for fundamental performance evaluation of the LDPC code.

4.4.2 Performance analysis

First, we compare the performance of the 5G NR Polar and LDPC code with the LTE Turbo code. The performance is evaluated in terms of BLER (block error rate) versus the SNR normalized to the energy per constellation symbol E_S/N_0 . The BLER is the most important performance metric of a channel code from a system level point of view. The simulated setup compares the performance for BPSK modulation over an AWGN channel for a medium block size of $B = 1024/1056$ and different code rates. Note that all codes only support a finite set of block sizes. For a meaningful comparison, we choose the code block size as similar as possible. Details on the simulation setup are summarized in Table 8.

The results are depicted in Figure 25. It can be observed that the LTE Turbo code performs worse for all code rates. In addition, the performance of the Turbo code becomes worse with increasing code rate. The reason for the second observation is that the base code rate of the Turbo code is $R = 1/3$ and random puncturing is used to perform rate matching to all higher code rates. However, in general, random puncturing performs well for low code rates and, for high code rates, *shortening* can yield better performance. Nevertheless, even for a code rate of $R = 1/3$, where no rate matching is applied, the performance of the Turbo code is significantly below the performance of its two competitors. Similar results were obtained for all other performance evaluations. Hence, turbo coding is not considered in all following performance comparisons. An inferior Turbo code performance was also the conclusion of the performance evaluation within 3GPP [36].

Table 8. Simulation parameters for comparison of Polar, LDPC and Turbo codes.

Channel	AWGN
Modulation	BPSK
Number of blocks	100,000
Block size B (Turbo/Polar/LDPC)	1056 / 1024 / 1056

² Available: <https://de.mathworks.com/help/lte/ref/lтетurboencode.html>

³ Available: <https://github.com/robmaunder/polar-3gpp-matlab>

⁴ Available: <https://github.com/vodafone-chair/5g-nr-ldpc>

Second, we compare the performance of the two 5G NR channel codes for the same simulation setup as given in The results are depicted in Figure 25. It can be observed that the LTE Turbo code performs worse for all code rates. In addition, the performance of the Turbo code becomes worse with increasing code rate. The reason for the second observation is that the base code rate of the Turbo code is $R = 1/3$ and random puncturing is used to perform rate matching to all higher code rates. However, in general, random puncturing performs well for low code rates and, for high code rates, *shortening* can yield better performance. Nevertheless, even for a code rate of $R = 1/3$, where no rate matching is applied, the performance of the Turbo code is significantly below the performance of its two competitors. Similar results were obtained for all other performance evaluations. Hence, turbo coding is not considered in all following performance comparisons. An inferior Turbo code performance was also the conclusion of the performance evaluation within 3GPP.

Table 8. The results are shown in Figure 26. The evaluation indicates that the performance is very similar for all investigated code rates of $R \in \{1/3, 1/2, 2/3, 3/4, 5/6\}$ and a block length of $B = 1024/1056$ for the Polar and LDPC code, respectively.

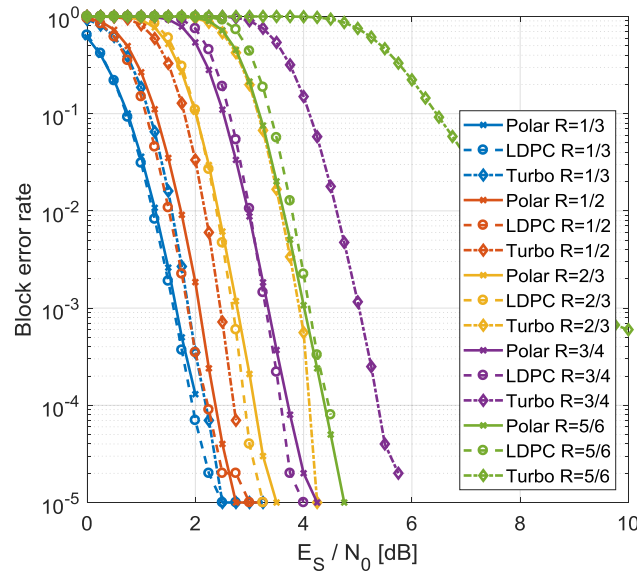


Figure 25. BLER performance comparison of Polar, LDPC and Turbo code for BPSK over AWGN.

⁵ In the literature, SCL decoding list sizes of 8/32 are commonly used. In addition, for performance evaluations of LDPC codes, 20 iterations are a common choice.

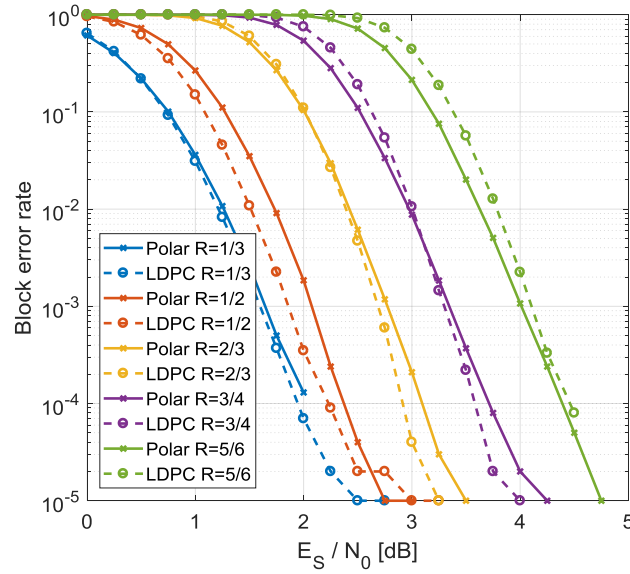


Figure 26. BLER performance comparison of 5G NR Polar and LDPC code for BPSK over AWGN.

Furthermore, we investigate the impact of the block size on the performance for 100,000 blocks for the same code rate of $R = 2/3$ and BPSK over AWGN. Table 9 provides an overview on the compared block sizes. The results are depicted in Figure 27. The evaluation indicates that the Polar code outperforms the LDPC code for small block sizes of 256/264 and 512/544. In contrast, for block sizes above 1024/1056, the LDPC code yields a lower BLER. Similar results were obtained during the comparison within 3GPP [37]. The superior performance of Polar codes for small block sizes is the reason why the Polar code is chosen as the channel coding scheme for the control channel, because the typical block sizes are comparatively small on this channel.

Table 9. Overview on the compared block sizes B for Polar and LDPC codes.

Polar	256	512	1024	2048	4096
LDPC	264	544	1056	2176	4224

Another parameter with a significant impact on the performance is the list size of the SCL Polar decoder and the number of iterations of the SPA of the LDPC decoder. The evaluation for list sizes and number of iterations in the range from 1 to 32 is depicted in Figure 28. The investigation reveals that the performance of the SCL Polar decoder grows significantly with the list size. With a list size of 8, the performance is already very close to saturation. In the literature on SCL Polar decoders, mostly list sizes of 8 or 32 are considered. Similarly, for the SPA LDPC decoder, 16 iterations yield a close to saturation performance. This justifies the generation of the previous results with a list size of 8 and 20 iterations for the SPA LDPC decoder, as given in Table 8.

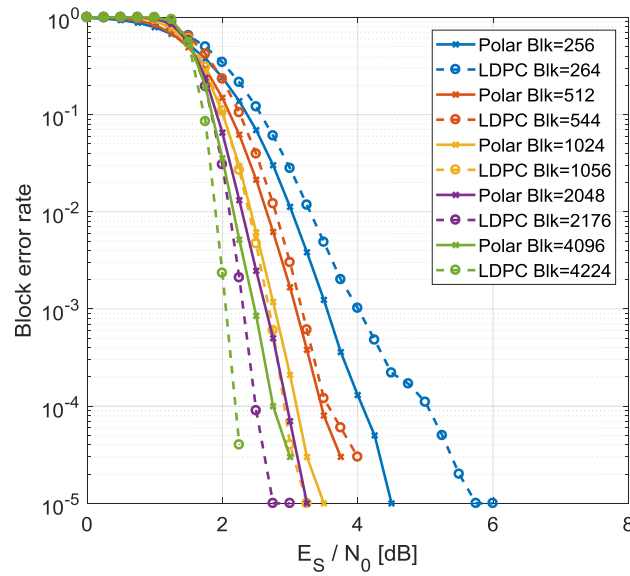


Figure 27. BLER comparison of 5G NR Polar and LDPC code for a code rate of $R = 2/3$ and different block sizes.

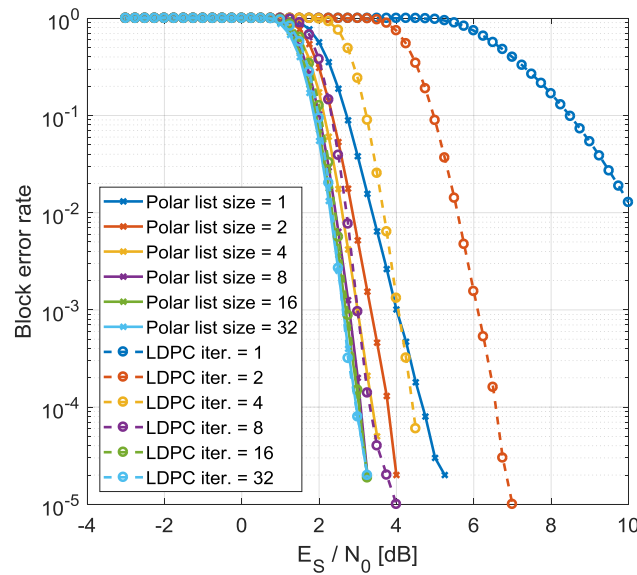


Figure 28. Evaluation of the BLER performance of the SCL Polar decoder and the SPA LDPC decoder for different list sizes and number of iterations, respectively. Results are obtained for 100,000 blocks of length $B=1024/1056$ with code rate $R=2/3$ for BPSK modulation over an AWGN channel.

For further performance evaluation of the Polar and LDPC code, the performance is investigated in a simulation including a full transmitter and receiver chain with GFDM modulation with practical signal processing algorithm in the receiver, e.g. ZF GFDM equalization over an AWGN channel. Details on the simulation setting and the GFDM configuration are given in Table 10. The constellation SER (symbol error rate) is depicted in Figure 29. As expected, the performance is identical for all FEC schemes and block sizes, because the SER is not affected by the channel codes which is employed on the bits afterwards. The performance in terms of BER (bit error rate) and BLER is shown in Figure 30 and Figure 31, respectively. The behavior is like the behavior without GFDM modulation. With increasing block size, the performance improves for both channel codes. For a block size of $B = 256/264$ the Polar code outperforms the LDPC code, whereas the LDPC code outperforms the Polar code for a block size of $B = 4096/4224$.

Table 10. Overview on the GFDM simulation settings.

Parameter	Setting
Modulation	GFDM
Sub-Carriers	16384
Sub-Symbols	4
Mapping	64-QAM
Code rate	$R = 3/4$
Interleaver	Random interleaving
Channel	AWGN

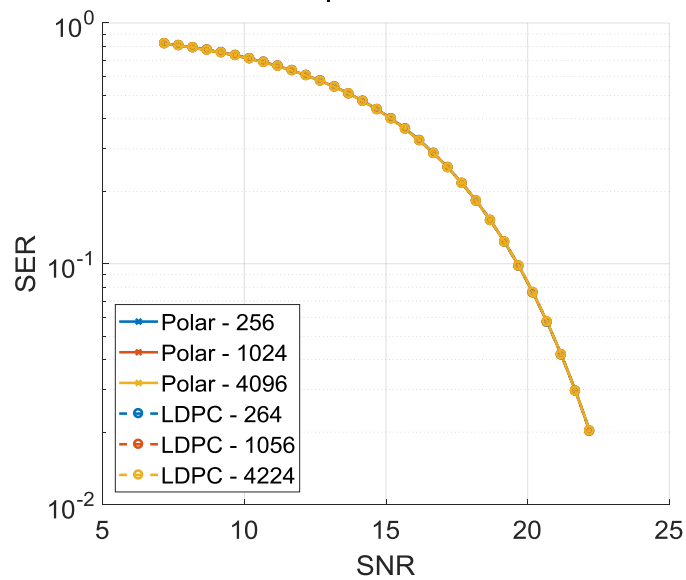


Figure 29. Comparison of QAM SER for Polar and LDPC code with different block sizes for GFDM modulation over an AWGN channel. As expected, the SER is independent of the channel code as well as the block size. Note that all curves are perfectly overlapping.

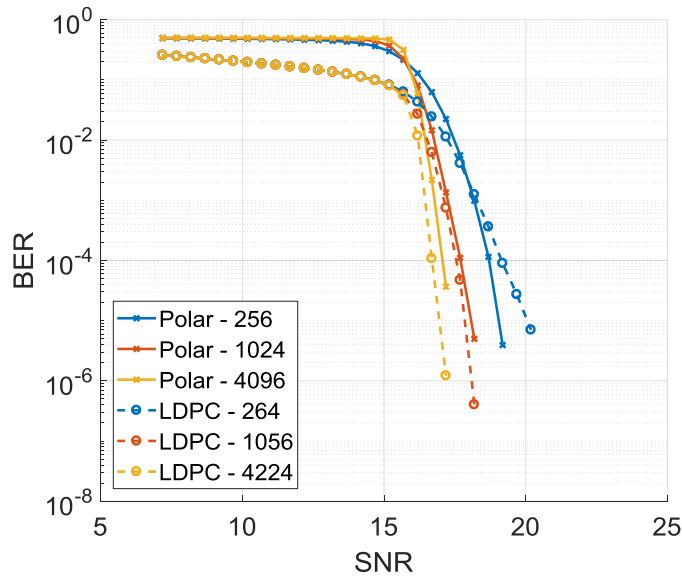


Figure 30. Comparison of BER for Polar and LDPC code with different block sizes for GFDM modulation over an AWGN channel.

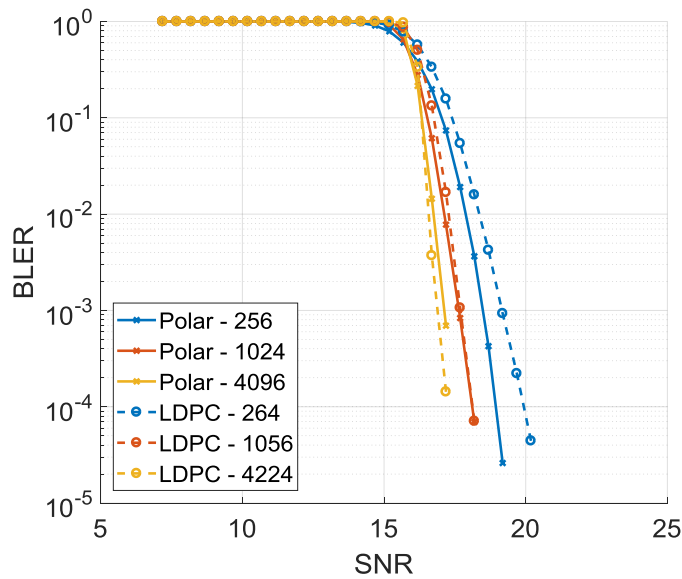


Figure 31. Comparison of BLER for Polar and LDPC code with different block sizes for GFDM modulation over an AWGN channel.

4.5 Complexity comparison

As already pointed out in the introduction of this section, the complexity of the channel coding is of great importance for the 5G-RANGE core use cases described in D2.1, because a lower complexity can directly reduce the cost and power consumption of the system. Both, low cost and low power consumption are important to enable a cost effective and, hence, practical system. Nevertheless, reduced complexity usually comes at the cost of a reduced performance. Therefore, it is important to find a good tradeoff between complexity and performance.

Evaluating the complexity of channel codes is a difficult task, because there is usually a performance complexity tradeoff, which not only depends on the channel code itself, but also on the chosen decoding algorithm. For the numerical evaluation in the previous section, we have used the best-

known algorithm in terms of performance. However, evaluating the complexity based on these algorithms and these implementations is not meaningful because:

- Runtime complexity in *MATLAB* does not necessarily correspond to complexity in an optimized hardware implementation;
- The *MATLAB* implementation is optimized for best performance and not for speed in order to investigate the fundamental performance limits of the channel codes;
- Practical systems usually implement a close to optimal, but sub-optimal algorithm to reduce complexity.

In the following, we briefly discuss the general theoretical complexity of Polar and LDPC decoders. Polar codes, as initially proposed by Arikan, have an encoding and SC decoding complexity of $O(B \log B)$ (B denotes the code block size, cf. Table 5), which is extremely good in terms of complexity [31]. However, SC decoding leaves a considerable performance gap as compared to more advanced decoding schemes. SCL decoding can significantly improve the performance at the cost of an L times higher decoding complexity of $O(L B \log B)$, where L denotes the size of the list [38]. CA-Polar codes can further improve performance with a small rate penalty, at nearly the same complexity [38].

For LDPC codes the optimal decoding algorithm is the SPA. However, in practice, this algorithm is nearly never implemented because of its high complexity. The most common lower complexity algorithm is the so-called MSA (min-sum-algorithm) [39]. Yet, because the loss in performance of MSA as compared to SPA is considerable, there are many variations of the MSA which try to improve the performance at slightly higher complexity. A common algorithm is e.g. the normalized MSA [40]. Performance and complexity can also be traded off by the choice of the maximum number of iterations of the decoding algorithm, as investigated in section 4.4.2. Another degree of freedom of LDPC decoders is the so-called schedule in which the updates between the variable and check nodes are exchanged and propagated through the factor graph [41].

In [36], the complexity of Polar, LDPC and Turbo codes is investigated. Nevertheless, the comparison is not very conclusive, because a unified comparison of the combined complexity in terms of additions, multiplications and look-up-table calls highly depends on the underlying hardware architecture. The authors find the complexity to be roughly similar but argue that LDPC codes can be implemented with comparatively low complexity and high flexibility because the decoding algorithms are usually iterative and can be parallelized efficiently. This is a disadvantage of traditional Polar decoders, which decode the code word serially, and hence their complexity and latency grows for longer code words. To overcome this, a lot of recent research focusses on parallel iterative decoding algorithms for Polar codes, mostly based on belief-propagation [42], [43].

However, a significant complexity reduction, without a necessarily significant performance penalty, as shown by the numerical evaluations in section 4.4.2, could be achieved by using a single channel code for both, the control and the transport channel. Since the channel code decoder is usually one of the most complex parts of a practical transceiver it seems logical to use a single coding scheme and, hence, a single decoder in the transceiver. Thereby we intend to reduce the transceiver complexity significantly with respect to channel coding when comparing a 5G-RANGE and a 5G NR transceiver.

4.6 Discussion and Future Perspectives

During the evaluation of modern channel codes, we have shown that Turbo codes are outperformed by Polar and modern LDPC codes in terms of BLER. Therefore, we will not consider them anymore as channel coding candidates for the 5G-RANGE PHY. The performance of Polar and LDPC codes is found to be similar; however, for smaller (larger) block sizes the performance of Polar (LDPC) codes is slightly superior. Similar results were obtained in the performance evaluation within 3GPP while working towards the 5G NR standardization. Our work provides a consistent and fair comparison of the most advanced currently known channel coding schemes over a wide range of practical code rates

and block sizes. We also possibly provide the first simulated performance comparison of 5G NR channel codes over GFDM AWGN channels.

Evaluation of the complexity of the channel codes is challenging because it highly depends on the underlying hardware and the actual decoding algorithm. Therefore, an in-depth evaluation is beyond the scope of this project. Nevertheless, we reduce the overall burden on the transceiver in terms of channel coding complexity by choosing a single channel coding scheme for both, the transport and the control channel. Since the performance gap of Polar and LDPC codes for short and long block sizes is very small, we do not think that this gap justifies the implementation of two channel coding schemes.

In the future of the project, the performance and complexity of Polar and LDPC codes will be further evaluated before finally choosing a channel coding scheme. As a result, it is planned to evaluate the performance in more detailed PHY simulations over the channel model of section 2, because it has to be ensured that the actual channel code meets the 5G-RANGE target specifications under the expected overall channel conditions. After that, a suitable MCS (modulation and coding scheme) table must be defined based on simulation results. All this work is planned to be part of D3.2.

5 EU projects on 5G PHY

During the last years, several projects targeting the 5G development has been supported by the European Commission. Some of these projects have developed solutions for the 5G PHY or have provided inputs for the 5G PHY development. The first relevant project in this aspect was METIS (Mobile and wireless communications Enablers for the Twenty-twenty Information Society) project. This project has provided the requirements for the most important 5G use cases and proposed a 5G architecture that encompass the entire network [44].

METIS II project, which is the follow up of METIS project, laid the base for the 5G PHY and MAC harmonization by providing insightful results for the 5G RAN (radio network access) [45]. The RAN architecture proposed by the METIS-II project was the baseline for the system architecture that is driving the 5G-RANGE PHY development. As already envisioned by METIS-II project, 5G AI (air interface) needs to present different variants in order to couple with the large number of possible use cases and 5G-RANGE is being developed to be compatible with the overall network architecture upon the concept of the network slicing.

5GNOW project, funded by the European Commission, has exploited different waveforms for the 5G PHY, each one with unique features that could benefit specific 5G use cases [46]. For instance, the low OOB emissions presented by FBMC is especially interesting for the 5G-RANGE core use cases. However, GFDM is also reported to achieve very low OOB emissions and furthermore has the advantage of being more flexible than FBMC, e.g., by covering other waveforms as corner cases of the GFDM configuration, as presented in section 3 of this report. 5GNOW also proposed a flexible framework for exploiting the time-frequency grid for different services. The principles of this framework are being used for the design of the 5G-RANGE frame, which will be presented in D3.2.

One5G is an ongoing project under the H2020 initiative that aims for promoting vertical use cases for 5G in urban and rural areas. The results to be achieved by the One5G project will impact in the future 5G standardization. One5G Deliverable 2.1 brings important KPIs for the remote area applications, which are similar to the 5G-RANGE KPIs. Cell coverage for rural areas is also target to 50 km, but 5G-RANGE throughput is higher. While 5G-RANGE targets for 100 Mbps/cell, One5G aims to achieve 50 Mbps/cell. Since One5G project has released only two deliverables so far, there is no information about the PHY and MAC layer proposals to achieve these KPIs. 5G-RANGE researchers will follow the One5G results in order to be aligned with the latest achievement of this relevant project.

6 Conclusions

In this document, a detailed description of the proposed channel model and discussions regarding to the waveforms and channel coding for the 5G-RANGE project were provided. The channel model was divided for two outdoor links, with distances between 20 m and 1 km, characterized by D2D links and the second one goes for distances of 1 km up to 50 km, characterized by the general case. Both models rely on measurements performed found in the literature. Simulations regarding the channel capacity were performed in order to analyze the upper bound for the proposed channel model capacity at the cell border.

About the waveforms, different techniques are being considered for the PHY air interface. GFDM, F-OFDM and B-OFDM are the most prominent candidates due to its characteristics regarding OOB emissions, spectrum efficiency and performance under time-variant and frequency-selective channels. The preliminary analysis presented in this document will be detailed in D3.2.

Regarding the channel code, a very extension comparison in terms of performance, block size and computational complexity between the possible channel codes (LDPC and Polar codes) for the 5G-RANGE using AWGN channels was performed. A unique performance evaluation of the channel codes combined with GFDM has also been presented in this document.

For the next deliverable D3.2 “Physical Layer of the 5G-RANGE – Part: 2” analyses of the channel capacity for different MIMO schemes in the 5G-MIMORA, including dual polarized antennas at the transmitter and receiver side will be performed. Also, a formal proposition of the waveform in the 5G-FlexNOW block and performance analyses of the 5G-ACRA using the proposed channel model will be present.

7 References

- [1] 5G-RANGE, ““Application and requirements report”, Deliverable 2.1, Work Package 2,” April 2018.
- [2] 3GPP TR 38.901, *Study on channel model for frequency form 0.5 to 100 GHz*, 2017.
- [3] S. Jaeckel, L. Raschkowski, K. Börner, L. Thiele, F. Burkhardt and E. Eberlein, “QuaDRiGa - Quasi Deterministic Radio Channel Generator, User Manual and Documentation,” 2017.
- [4] Ericsson & Telstra - A, *R1 - 166599, Measurements for extreme rural scenario*, Göterberg, 2017.
- [5] Ericsson & Telstra - C, *R1-167452 Path loss model for extreme rural scenario*, Göteborg, 2016.
- [6] Ericsson & Telstra - B, *R1-167451 Channel model for extreme rural scenario*, Göteborg, 2016.
- [7] S. Chandrasekharan, A. Al-Hourani, K. Magowe, L. Reynaud and S. Kandeepan, “Propagation Measurements for D2D in Rural Areas,” *IEEE ICC*, 2015.
- [8] A. W. Bowman, “An alternative method of cross-validation for the smoothing of density estimates.,” *Biometrika*, pp. 353-360.
- [9] J. Fischer, M. Grossmann, W. Felber, M. Landmann and A. Heuberger, “A Novel Delay Spread Distribution Model for VHF and UHF Mobile-to-Mobile Channels,” in *EuCAP*, 2013.
- [10] METIS, *METIS Channel Modes Deliverable D1.4*, 2015.
- [11] 3GPP R1-132803, *WF on D2D Doppler Modeling*, 2013.
- [12] J. W. T. a. W. A. L. R. McGill, “Variations of box plots,” *The American Statistician*, vol. 32, pp. 12-16, 1978.
- [13] ITU-R, “REPORT ITU-R BT.2035-2 Guidelines and techniques for the evaluation of digital terrestrial television broadcasting systems including assessment of their coverage areas,” 2008.
- [14] J. S. U. M. S. S. C. J. K. H. R. P. Y. H. K. Sung Hyun Hwang, “Design and Verification of IEEE 802.22 WRAN Physical Layer,” in *2008 3rd International Conference on Cognitive Radio Oriented Wireless Networks and Communications (CrownCom 2008)*, Singapore, Singapore, 2008.
- [15] M. J. a. J. M. Javad Abdoli, “Filtered OFDM: A New Waveform for Future,” in *Signal Processing Advances in Wireless Communications (SPAWC), 2015 IEEE 16th International Workshop on*, Stockholm, Sweden, 2015.
- [16] N. Michailow, “Generalized Frequency Division Multiplexing for 5th Generation Cellular Networks,” *IEEE Transactions on Communications*, pp. 3045-3061, September 2014.
- [17] M. Matthé, N. Michailow, I. Gaspar and G. Fettweis, “Influence of pulse shaping on bit error rate performance and out of band radiation of Generalized Frequency Division Multiplexing,” *IEEE International Conference on Communications Workshop*, pp. 43-48, June 2014.
- [18] I. Gaspar, L. Mendes, M. Matthé, N. Michailow, D. Zhang, A. Alberti and G. Fettweis, “GFDM - A Framework for Virtual PHY Services in 5G Networks,” *CoRR*, August 2015.
- [19] M. Matthé, L. Mendes, I. Gaspar, N. Michailow, D. Zhang and G. Fettweis, “Multi-user time-reversal STC-GFDMA for future wireless networks,” *EURASIP Journal on Wireless*

Communications and Networking, p. 132, September May 2015.

- [20] T. Ching-Lun, S. Borching and J. Cai, “Frequency-Domain Decoupling for MIMO-GFDM Spatial Multiplexing,” *CoRR*, August 2018.
- [21] I. Gaspar, M. Matth  , N. Michailow, L. Mendes, D. Zhang and G. Fettweis, “Transceiver using Precoded Data and Low-complexity Multiplication in Time Domain,” *CoRR*, August 2015.
- [22] 5GNOW Project, "D3.1: 5G Waveform Candidate Selection," 2014.
- [23] D. Zhang, M. Matth  , L. Mendes and G. Fettweis, “A Study on the Link Level Performance of Advanced Multicarrier Waveforms Under MIMO Wireless Communication Channels,” *IEEE Transactions on Wireless Communications*, vol. 16, no. 4, pp. 2350-2365, April 2017.
- [24] 3GPP, *Technical specification (TS) 36.212 - E-UTRA; Multiplexing and channel coding*, 2018.
- [25] 3GPP, *Technical specification (TS) 38.212 - NR; Multiplexing and channel coding*, 2017.
- [26] T. Richardson and R. Urbanke, *Modern Coding Theory*, Cambridge University Press, 2008.
- [27] R. G. Gallager, *Low-Density Parity-Check Codes*, MIT Press, 1963.
- [28] T. Richardson and S. Kudekar, “Design of Low-Density Parity Check Codes for 5G New Radio,” *IEEE Communications Magazine*, vol. 56, pp. 28-34, 2018.
- [29] F. Hamidi-Sepehr, A. Nimbalkar and G. Ermolaev, “Analysis of 5G LDPC Codes Rate-Matching Design,” in *2018 IEEE 87th Vehicular Technology Conference (VTC Spring)*, Porto, 2018.
- [30] P. Frenger, S. Parkvall and E. Dahlman, “Performance comparison of HARQ with Chase combining and incremental redundancy for HSDPA,” in *IEEE 54th Vehicular Technology Conference. VTC Fall 2001*, Atlantic City, 2001.
- [31] E. Arikan, “Channel Polarization: A Method for Constructing Capacity-Achieving Codes for Symmetric Binary-Input Memoryless Channels,” *IEEE Transactions on Information Theory*, vol. 55, pp. 3051-3073, 2009.
- [32] C. Leroux, I. Tal, A. Vardy and W. J. Gross, “Hardware architectures for successive cancellation decoding of polar codes,” in *2011 IEEE International Conference on Acoustics, Speech and Signal Processing (ICASSP)*, Prague, 2011.
- [33] G. Berhault, C. Leroux, C. J  go and D. Dallet, “Partial sums generation architecture for successive cancellation decoding of polar codes,” in *SiPS 2013 Proceedings*, Taipei City, 2013 .
- [34] H. Z. e. al., “Parity-Check Polar Coding for 5G and Beyond,” in *IEEE International Conference on Communication*, Kansas City, 2018 .
- [35] E. Sharon, S. Litsyn and J. Goldberger, “An efficient message-passing schedule for LDPC decoding,” in *23rd IEEE Convention of Electrical and Electronics Engineers in Israel*, Tel-Aviv, 2004.
- [36] Nokia, Alcatel-Lucent Shanghai Bell, *R1-162897: Performance and complexity of Turbo, LDPC and Polar codes*, Busan, 2016.
- [37] Huawei, HiSilicon, *R1-1611256: Performance evaluation of channel codes for small block sizes*, Reno, 2016.
- [38] I. Tal and A. Vardy, “List Decoding of Polar Codes,” *IEEE Transactions on Information Theory*, vol. 61, pp. 2213-2226, 2015.

-
- [39] M. P. C. Fossorier, M. Mihaljevic and H. Imai, “Reduced complexity iterative decoding of low-density parity check codes based on belief propagation,” *IEEE Transactions on Communications*, vol. 47, pp. 673-680, 1999.
 - [40] J. Chen and M. P. C. Fossorier, “Near optimum universal belief propagation based decoding of low-density parity check codes,” *IEEE Transactions on Communications*, vol. 50, pp. 406-414, 2002.
 - [41] E. Sharon, S. Litsyn and J. Goldberger, “Efficient Serial Message-Passing Schedules for LDPC Decoding,” *IEEE Transactions on Information Theory*, vol. 53, pp. 4076-4091, 2007.
 - [42] C. Schnelling, Y. Amraue and A. Schmeink, “On iterative decoding of polar codes: Schedule-dependent performance and constructions,” in *55th Annual Allerton Conference on Communication, Control, and Computing*, Monticello, IL, USA, 2017.
 - [43] A. Elkelesh, M. Ebada, S. Cammerer and S. ten Brink, “Belief Propagation List Decoding of Polar Codes,” *IEEE Communications Letters*, vol. 22, pp. 1536-1539, 2018.
 - [44] H. Droste and et. al., “The METIS 5G Architecture: A Summary of METIS Work on 5G Architectures,” in *2015 IEEE 81st Vehicular Technology Conference (VTC Spring)*, Glasgow, UK, 2015.
 - [45] P. Marsch and I. Silva, “Preliminary Views and Initial Considerations on 5G RAN Architecture and Functional Design,” 5G-PPP, 2016.
 - [46] G. Wunder and et al, “5GNOW: non-orthogonal, asynchronous waveforms for future mobile applications,” *IEEE Communications Magazine*, vol. 52, no. 2, pp. 97 - 105, 2014.
 - [47] N. e. a. Bhushan, “5G Air Interface System Design Principles,” *IEEE Wireless Communications*, vol. 24, pp. 6 - 8 , 2017.
 - [48] 3GPP, *Technical Specification (TS) 38.201; NR; Physical layer; General description. Release 15*, 2018.
 - [49] 3GPP, *Technical specification (TS) 38.211; Evolved Universal Terrestrial Radio Access (E-UTRA); Physical channels and modulation, Release15*, 2018.
 - [50] D. Nogu  t, M. Gautier and V. Berg, “Advances in opportunistic radio technologies for TVWS,” *EURASIP Journal on Wireless Communications and Networking*, 15 11 2011.

Annex A

The angular spread is given by [3]

$$\psi_{\text{rms}} = \sqrt{\sum_{i=1}^N P_i \cdot \psi_i^2 - \left(\sum_{i=1}^N P_i \cdot \psi_i \right)^2} \quad (30)$$

and the scaled angles of the desired model are given by

$$\psi_{n,\text{SCALED}} = \frac{\psi_{\text{rms,DESIRED}}}{\psi_{\text{rms,MODEL}}} \cdot \psi_{n,\text{MODEL}} \quad (31)$$

where

- $\psi_{\text{rms,DESIRED}}$ is the RMS desired angular spread;
- $\psi_{\text{rms,MODEL}}$ is the RMS angular spread from the model CDL from the CDL given in [1];
- $\psi_{n,\text{SCALED}}$ is the scaled angles of the desired model.

Likewise, the delay spread is given by [2]

$$\tau_{\text{rms}} = \sqrt{\sum_{i=1}^N P_i \cdot \tau_i^2 - \left(\sum_{i=1}^N P_i \cdot \tau_i \right)^2} \quad (32)$$

and the delays of the desired model are given by

$$\tau_{n,\text{DESIRED}} = \frac{\tau_{\text{rms,DESIRED}}}{\tau_{\text{rms,MODEL}}} \cdot \tau_{n,\text{MODEL}} \quad (33)$$

where

- $\tau_{\text{rms,DESIRED}}$ is the RMS desired delay spread;
- $\tau_{\text{rms,MODEL}}$ is the RMS delay spread from the model CDL from the CDL given in [1];
- $\tau_{n,\text{SCALED}}$ is the scaled delays of the desired model.

Annex B

Table 11. CDL-A model with scaled delays and angles for the general case.

	DS [ns]	k [linear]	ASD [°]	ASA [°]	ZSD [°]	ZSA [°]
	100	0	1	30	0.1	1
Cluster	Delay [ns]	Normalized Power [dB]	AOD [°]	AOA [°]	ZOD [°]	ZOA [°]
1	0	-13.40	-2.422	15.482	0.177	6.009
2	38.19	0.00	-0.057	-46.083	0.328	4.375
3	40.25	-2.20	-0.057	-46.083	0.328	4.375
4	58.68	-4.00	-0.057	-46.083	0.328	4.375
5	46.10	-6.00	1.227	23.117	0.430	4.504
6	53.75	-8.20	1.227	23.117	0.430	4.504
7	67.08	-9.90	1.227	23.117	0.430	4.504
8	57.50	-10.50	1.652	-0.543	0.529	2.257
9	76.18	-7.50	-1.111	-12.645	0.194	2.684
10	153.75	-15.90	2.154	28.428	0.093	1.442
11	189.78	-6.60	-1.129	15.663	0.445	2.818
12	222.42	-16.70	1.833	-34.977	0.604	1.246
13	217.18	-12.40	-2.081	8.028	0.533	2.358
14	249.42	-15.20	-2.339	23.117	0.554	6.857
15	251.19	-10.80	-1.767	-2.113	0.166	5.626
16	305.82	-11.30	-1.850	-6.941	0.142	5.880
17	408.10	-12.70	2.250	-14.244	0.152	5.904
18	445.79	-16.20	2.018	33.317	0.570	1.562
19	456.95	-18.30	1.805	43.608	0.038	1.303
20	479.66	-18.90	-1.613	46.867	0.059	0.728
21	500.66	-16.60	-2.096	30.782	0.605	6.996
22	530.43	-19.90	1.720	-45.811	0.080	7.221
23	965.86	-29.70	-0.764	16.659	0.510	7.480
Per cluster parameters						
Parameters		c_{ASD} [°]	c_{ASA} [°]	c_{ZSD} [°]	c_{ZSA} [°]	XPR [dB]
Value		5	11	3	3	10

Table 12. CDL-D with scaled delays and angles for the general case.

	DS [ns]	k [linear]	ASD [°]	ASA [°]	ZSD [°]	ZSA [°]
	100	6.37	1	30	0.1	1
Cluster	Delay [ns]	Normalized Power [dB]	AOD [°]	AOA [°]	ZOD [°]	ZOA [°]
1	0	-0.2	0	-72.816	4.408	69.946
1	0	-13.5	0	-72.816	4.408	69.946
2	3.5	-18.8	5.714	36.084	3.827	74.580
3	61.2	-21	5.714	36.084	3.827	74.580
4	136.3	-22.8	5.714	36.084	3.827	74.580
5	140.5	-17.9	0.833	65.939	4.364	68.143
6	180.4	-20.1	0.833	65.939	4.364	68.143
7	259.6	-21.9	0.833	65.939	4.364	68.143
8	177.5	-22.9	2.216	-55.421	4.408	67.114
9	404.2	-27.8	-4.132	30.138	3.956	63.166
10	793.7	-23.6	-2.107	51.659	4.086	67.199
11	942.4	-24.8	3.369	-48.382	4.646	74.666
12	970.8	-30	-8.462	-3.681	3.594	60.591
13	1252.5	-27.7	4.945	-33.900	3.871	62.565
Per cluster parameters						
Parameters		c_{ASD} [°]	c_{ASA} [°]	c_{ZSD} [°]	c_{ZSA} [°]	XPR [dB]
Value		5	8	3	3	11

Annex C

Table 13. CDL-A with scaled delays and angles for D2D.

	DS [ns]	k [linear]	ASD [°]	ASA [°]	ZSD [°]	ZSA [°]
	500	0	9	53.3	8	18
Cluster	Delay [ns]	Normalized Power [dB]	AOD [°]	AOA [°]	ZOD [°]	ZOA [°]
1	0.00	-13.4	-21.80	28.54	14.14	108.16
2	190.9	0	-0.51	-84.95	26.25	78.75
3	201.3	-2.2	-0.51	-84.95	26.25	78.75
4	293.4	-4	-0.51	-84.95	26.25	78.75
5	230.5	-6	11.04	42.61	34.37	81.08
6	268.7	-8.2	11.04	42.61	34.37	81.08
7	335.4	-9.9	11.04	42.61	34.37	81.08
8	287.5	-10.5	14.87	-1.00	42.31	40.63
9	380.9	-7.5	-10.00	-23.31	15.55	48.30
10	768.8	-15.9	19.39	52.40	7.44	25.96
11	948.9	-6.6	-10.16	28.87	35.61	50.72
12	1112.1	-16.7	16.50	-64.47	48.34	22.43
13	1085.9	-12.4	-18.73	14.80	42.65	42.44
14	1247.1	-15.2	-21.05	42.61	44.28	123.43
15	1255.9	-10.8	-15.90	-3.89	13.30	101.26
16	1529.1	-11.3	-16.65	-12.79	11.38	105.83
17	2040.5	-12.7	20.25	-26.26	12.20	106.27
18	2229.0	-16.2	18.16	61.41	45.58	28.12
19	2284.7	-18.3	16.24	80.38	3.04	23.46
20	2398.3	-18.9	-14.52	86.39	4.70	13.11
21	2503.3	-16.6	-18.86	56.74	48.37	125.93
22	2652.1	-19.9	15.48	-84.45	6.39	129.99
23	4829.3	-29.7	-6.88	30.71	40.82	134.64
Per cluster parameters						
Parameters		c_{ASD} [°]	c_{ASA} [°]	c_{ZSD} [°]	c_{ZSA} [°]	XPR [dB]
Value		5	11	3	3	10

Table 14. CDL-D with scaled delays and angles for D2D.

	DS [ns]	k [linear]	ASD [°]	ASA [°]	ZSD [°]	ZSA [°]
	500	6.37	9	53.3	8	18
Cluster	Delay [ns]	Normalized Power [dB]	AOD [°]	AOA [°]	ZOD [°]	ZOA [°]
1	0.00	-0.2	0.00	-134.22	116.42	168.38
1	0.00	-13.5	0.00	-134.22	116.42	168.38
2	17.5	-18.8	51.42	66.52	85.04	77.54
3	306.0	-21	51.42	66.52	85.04	77.54
4	681.5	-22.8	51.42	66.52	85.04	77.54
5	702.5	-17.9	7.49	121.55	114.01	137.86
6	902.0	-20.1	7.49	121.55	114.01	137.86
7	1298.0	-21.9	7.49	121.55	114.01	137.86
8	887.5	-22.9	19.95	-102.16	116.42	120.43
9	2021.0	-27.8	-37.18	55.55	92.04	53.59
10	3968.5	-23.6	-18.97	95.22	99.04	121.88
11	4712.0	-24.8	30.32	-89.18	7.85	78.99
12	4854.0	-30	-76.16	-6.79	72.49	10.01
13	6262.5	-27.7	44.51	-62.49	87.45	43.42
Per cluster parameters						
Parameters		c_{ASD} [°]	c_{ASA} [°]	c_{ZSD} [°]	c_{ZSA} [°]	XPR [dB]
Value		5	8	3	3	11